LBL-23523 c.2

Center for Advanced Materials

CAM REPORT

RECEIVED
LAWRENCE
BERKELEY LABORATORY

JUL 31 1987

LIBRARY AND
DOCUMENTS SECTION

BACKSCATTERING MÖSSBAUER SPECTRUM AND SPECIMEN THICKNESS

Z. Mei
(M.S. Thesis)

May 1987

TWO-WEEK LOAN COPY

This is a Library Circulating Copy which may be borrowed for two weeks.

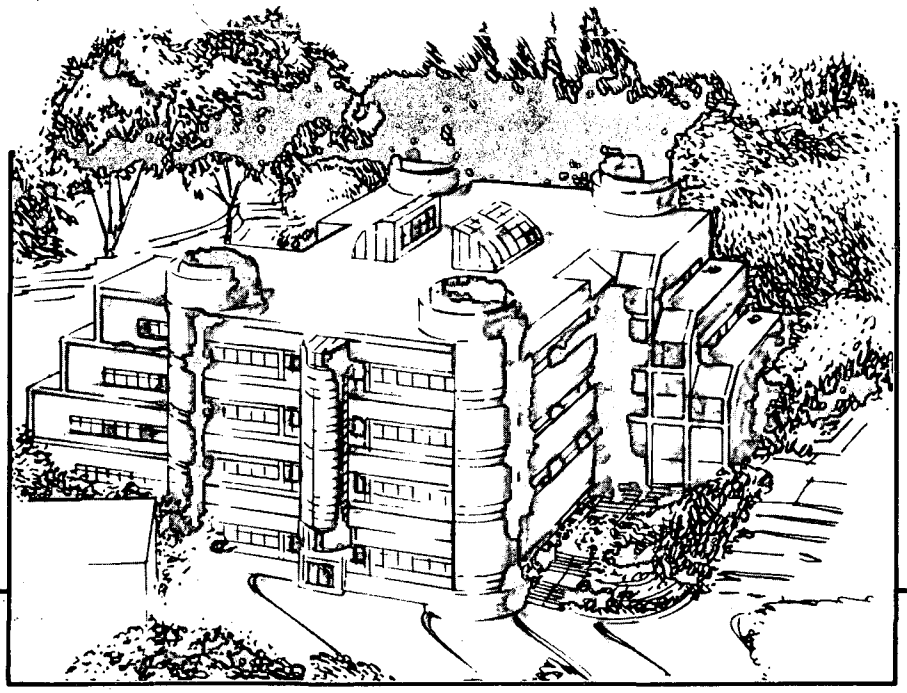

Materials and Chemical Sciences Division

Lawrence Berkeley Laboratory • University of California

ONE CYCLOTRON ROAD, BERKELEY, CA 94720 • (415) 486-4755

Prepared for the U.S. Department of Energy under Contract DE-AC03-76SF00098

LBL-23523 c.2

DISCLAIMER

This document was prepared as an account of work sponsored by the United States Government. While this document is believed to contain correct information, neither the United States Government nor any agency thereof, nor the Regents of the University of California, nor any of their employees, makes any warranty, express or implied, or assumes any legal responsibility for the accuracy, completeness, or usefulness of any information, apparatus, product, or process disclosed, or represents that its use would not infringe privately owned rights. Reference herein to any specific commercial product, process, or service by its trade name, trademark, manufacturer, or otherwise, does not necessarily constitute or imply its endorsement, recommendation, or favoring by the United States Government or any agency thereof, or the Regents of the University of California. The views and opinions of authors expressed herein do not necessarily state or reflect those of the United States Government or any agency thereof or the Regents of the University of California.

Backscattering Mössbauer Spectrum and Specimen Thickness

(Master Thesis)

Zequn Mei

Materials Science and Mineral Engineering Department
University of California, Berkeley
and
Center for Advanced Materials
Materials and Chemical Sciences Division
Lawrence Berkeley Laboratory
University of California
Berkeley, California 94720

May, 1987

ACKNOWLEDGMENTS

I would like to thank Prof. J. W. Morris, Jr very very much. He supervised and generously supported this research. Discussion with him in the group seminar helped me to understand most difficult part of this research.

I am specially grateful to Prof. B. Fultz. He gave me enormous guidance and help from the beginning to the end of this research. He had the original ideal of this research, and provided numerous suggestions afterwards.

I am grateful to Dr. Charles Violet in LLNL and Gerard Vurens in Prof. Somajai's group. They are experts in Mössbauer spectrometer, their suggestions are valuable.

I am grateful to all the people in Prof. Morris's group, it is impossible to list all the favours they did me. Especially I would like to thank Jin Chan, Dana Tribula, Sue Vincent, and Dan Dietderich.

I am grateful to Prof. Alan M. Portis and Prof. Thomas M. Devine, Jr. They are committee members of my thesis. They read and corrected the thesis, and provided a lot of valuable opinions.

I give my special thanks to my wife Ping, my Mother, and Brother for everything they gave to me.

This work is supported by the director, Office of Energy Research, Office of Fusion Energy, Development and Technology Division of U.S. Department of Energy, under contract #DE-AC 03-76-SF00098.

Table of Contents

1. Introduction 1

2. Background 3

3. Theory 6

   3.1. Analysis of γ-ray backscattering Mössbauer spectrum 6

   3.2. Analysis of conversion x-ray backscattering Mössbauer spectrum 12

4. Experiments 17

   4.1. γ-ray BMS of Be containing Fe impurities 17

   4.2. Conversion x-ray BMS of pure Fe 19

5. Results and Discussion 20

6. Conclusions 23

Reference 24

Appendix 1 26

List of Symbols 33

List of Tables 35

Tables 36

List of Figures 44

Figures 45

1. INTRODUCTION

Mössbauer spectroscopy is a useful technique for phase identification and chemical analysis in metallurgy. The work by Fultz [ref.1] is a good example of how the technique can be successfully used in characterizing Fe-Ni-X alloys, where X are Cr, Si, Mn and etc.. However, a critical problem in utilizing Mössbauer spectroscopy for quantitative analysis is the specimen thickness correction. This problem was relatively well explained [ref. 3-9] and solved [ref. 10-16] for the transmission Mössbauer spectrum (TMS), but not for the backscattering Mössbauer spectrum (BMS).

The goal of the quantitative analysis is to relate the amplitude or the area underneath a peak in a Mössbauer spectrum to the phase or chemical element that induces the peak. For a thin specimen, the peak amplitude or the area underneath have a linear relation with the amount of the phase or chemical element. But for a very thick specimen, the linear relation is no longer valid; each individual Mössbauer element does not contribute to the peak the same amount as it does for a thin specimen. A thickness correction is necessary.

There are two ways to proceed the thickness correction: experimental calibration or theoretical calculation. The latter one requires a theory to compute the peak amplitude or the area underneath as a function of the specimen thickness for a given phase.

This project was initiated as a result of my curiosity about the computational results of Dr. Narendra K. Jaggi [ref.2]. Figure 1 in Chapter 4 of his thesis showed non-monotonic saturation of the peak amplitude with specimen thickness for the stainless steel backscattering Mössbauer spectra (see Figure 1 in this thesis), and Figure 2 in his thesis (also Figure 2 in this thesis) actually showed that the amplitude becomes negative as the thickness exceeds a certain value for the backscattering Mössbauer spectra of Fe in coal. This is a surprising result because if it is true any attempt at quantitative analysis based on peak amplitude is futile as the peak amplitude may be negative!

The first portion of this work was to verify Jaggi's computation experimentally. In the process of computation, a simple criterion was found for the occurrence of negative amplitude BMS. This criterion indicated that Be metal with Fe impurity is the most promising available material for achieving negative amplitude BMS. The backscattering Mössbauer spectra of Be with < 1 wt % of Fe collected by us showed a transition from the "peak" to the "dip" with increase in the specimen thickness.

The second result of this work is that the non-monotonic saturation of peak amplitude with the scatterer thickness also occurs in conversion x-ray backscattering Mössbauer spectroscopy, but for a different reason. Bearing in mind the similarities and differences between the γ-ray BMS and x-ray BMS, Bara-Jaggi's theory of γ-ray BMS has been modified, and applied to the x-ray BMS. The numerical calculation based on the modified theory showed that the peak amplitude of x-ray BMS increases with specimen thickness non-monotonically. The mössbauer spectra collected on pure Fe specimens with a range of thickness proved the theory.

2. BACKGROUND

Even though Mössbauer spectroscopy (MS) is becoming a common technique in the field of metallurgy, it will be convenient for the reader of this thesis if important concepts in MS are briefly explained here. Several text books on Mössbauer spectroscopy [ref.17,18] provide more details.

Mössbauer spectroscopy makes use of the Mössbauer effect (ME) discovered by Rudolf Mössbauer in 1957. The ME is a mechanism to achieve nuclear resonance. Nuclear resonance occurs when a γ-ray photon emitted by a de-exciting nucleus is resonantly absorbed by exciting another nucleus of the same isotope. Nuclear resonance had never been achieved experimentally before Rudolf Mössbauer's experiment. The early failures were due to the recoil of the nuclei, which occurs when isolated nuclei emit or absorb γ-rays. This recoil occurs to balance the change of momentum during the emission or absorption. The energy taken away by the recoil of the nuclei spoiled exact coincidence of the incident γ–ray energy with the resonant energy of the absorber nuclei, and so made the nuclear resonance impossible. But R. Mössbauer succeeded in realizing nuclear resonance "recoillessly" by imbedding the nuclei of the γ-ray emitter and absorber into a well-bound crystalline solid. The beauty of the ME is that the whole crystalline solid recoils instead of the individual nucleus, so that the energy taken away by recoil will be negligible, since the recoil energy is inversely proportional to the mass of the object that recoils. Detailed calculations [chapter 2 in ref.18] give a recoilless fraction, f, of the γ-rays emitted that depends on the lattice dynamics of the crystal in which the Mössbauer nuclei are imbedded.

A simple layout of the ^{57}Fe Mössbauer spectrometer is shown in Figure 3. In the γ-ray source, ^{57}Co nuclei decay radioactively with a half life of 270 days to ^{57}Fe which are in excited states; de-excitations to the ground state of the ^{57}Fe nuclei produce γ-rays with several energies. The resulting 14.4 keV γ-rays (from the first excited state to the ground

state) can excite ^{57}Fe in the specimen we want to study with much higher probability than the other high energy γ-rays can do. To accomplish nuclear resonance, the source is vibrated by a driver, usually for experimental simplicity, the velocity changes with time as a triangular waveform. The purpose of such vibration of the γ-ray source is to modulate γ-ray energy by the Doppler effect. If E_0 is the γ-ray energy when the vibrating velocity is zero, the energy of the γ-rays produced by a vibrating source will be $E_0 (1 + v / c)$ when the velocity is v, where c is light speed. E_0 is the energy difference between the excited and ground states of a ^{57}Fe nuleus in the γ-ray source, while the resonant energy, E_1, is the energy difference of the excited and ground states of a ^{57}Fe nucleus in the specimen. E_0 is usually slightly different from E_1, because the hyperfine interaction of the nuclear positive charge with its electronic environment changes the nuclear energy level. Since the matrix materials (alloy compositions) for ^{57}Fe in the γ-ray source and in the specimen are different, so are the hyperfine interactions, and therefore E_0 and E_1. The Doppler effect-induced γ-ray energy modulation can cause $E_0 (1 + v / c)$ to match E_1 at a certain v called the resonant velocity; velocities that do not cause matching are called off-resonant velocities. Generally v is called the Doppler velocity. A Mössbauer spectrum is a plot of the number of γ-rays received by the detector as a function of the Doppler velocity.

There are two basic experimental geometries for MS, transmission Mössbauer spectroscopy and backscattering Mössbauer spectroscopy. TMS has the absorber between the γ-ray source and detector, while BMS collects the γ-rays being scattered back by the absorber. These backscatted γ-rays are actually re-emitted γ-rays as a result of de-excitation of the excited ^{57}Fe in the specimen. TMS and BMS are complementary in the sense that TMS shows minimum counts (dip) of γ-rays at the resonant velocity while BMS shows maximum counts (peak) at the resonant velocity.

There are three kinds of BMS. Besides the above-mentioned γ-ray BMS, the other two are conversion x-ray and conversion electron BMS. As an alternative to re-emission of a γ-ray, the de-excitation of the excited ^{57}Fe in the absorber may happen by an internal

conversion process. In this process the internal orbital electrons are ejected by the energy released from the de-excitation. The electron orbit vacancy thus produced is refilled by an outer orbital electron, so that x-rays and Auger electrons are produced. The spectrum of the ejected electrons (so called "internal conversion electrons") or x-rays as a function of the Doppler velocity contains the same information about the energy levels of the ^{57}Fe in the absorber that the γ-ray BMS provides. The only difference between the conversion electron BMS, x-ray BMS and γ-ray BMS is the penetration depth; the conversion electron BMS reflects information from the surface of the specimen.

The absorption peak for the nuclear resonant absorption of γ-rays is extremely narrow and sharp, (e.g. for ^{57}Fe its width is about 9.78×10^{-9} eV), and is of the same order as the hyperfine interaction between the nucleus and its electronic environment. MS thus provides a new way to characterize the hyperfine interaction. In the field of metallurgy MS is usually used as a phase identification and chemical analysis technique. The principle is that different phases or chemical elements change the nuclear energy levels of ^{57}Fe differently (some may shift the nuclear level, or may change a single level to a doublet or sextet), which gives each phase a unique spectrum as its fingerprint.

3. THEORY

This section includes two parts. In the first part, Bara's theory of γ-ray BMS for finite thickness scatterers is briefly explained. Based on that theory, a simple expression of the criterion for negative amplitude BMS is developed. In the second part, a new theory of x-ray BMS for a scatterer of finite thickness is derived, the peak amplitude of the x-ray BMS as a function of the scatterer thickness is then calculated.

3.1. Analysis of γ-ray BMS

3.1.1. Bara's theory of γ-ray BMS for a scatterer of finite thickness

The mathematical theory of γ-ray BMS for finite thickness scatterers was first provided by P. Debrunner and R. J. Morrison (ref.19), and later was expanded by B. Balke and G. R. Hoy (ref.20). J. J. Bara is the first person who solved the problem properly (ref. 21-23). Based on Bara's theory, Narendra K. Jaggi further studied this issue (ref.2).

Bara proposed that the γ-rays being scattered by a scatterer containing Mössbauer elements result from seven contributions. The γ–rays from the source have both a recoilless part and non-recoilless part; they are the results of recoilless emission and non-recoilless emission of γ-rays through de-excitation of ^{57}Fe. As mentioned previously, only the recoilless γ-rays can be resonantly absorbed by the ^{57}Fe in the scatterer. There are two kinds of scattering processes: resonant scattering, i.e. the γ-rays being resonantly absorbed and subsequently re-emitted, and non-resonant scattering, in particular, Rayleigh scattering (the incident γ-rays collide with the atoms in the scatterer and are scattered; another way of looking at Rayleigh scattering is to consider it as a collision of incident γ-rays with tightly-bound electrons) and Compton scattering (collision of incident γ-rays with loosely-bound electrons). In summary, the above-mentioned seven contributions are: the recoilless part of the incident γ–rays being scattered by nuclear resonance recoillessly (1) and non-

recoillessly (2), by Rayleigh scattering recoillessly (3) and non-recoillessly (4) , and by Compton scattering (5); the non-recoilless part of the incident γ-rays being scattered by Rayleigh (6) and Compton (7) scattering.

There are two kinds of absorption: resonant absorption, i.e. nuclear resonant absorption; and non-resonant absorption, including photoelectronic absorption, Rayleigh scattering absorption, and Compton scattering absorption. γ-rays are "really" absorbed by the photoelectronic absorption, but are only scattered by Rayleigh and Compton scattering absorptions.

The mathematical expressions listed in Table 1 for the seven contributions can be derived with the aid of Figure 5. First of all, a scatterer of finite thickness can be divided into numerous layers with infinitesimal thickness; integrating the backscattered γ-rays from each layer will give the total backscattered γ-ray intensity. For each layer, the incident recoilless and non-recoilless γ-rays should be considered separately. The incident recoilless γ-rays have the well-known intensity vs energy distribution of the Lorentzian form [ref.24]. The Lorentzian function is shown in Figure 5, and is characterized by the symmetry center E_0 and full width at half height, Γ. Before the recoilless incident γ-rays have reached an embedded layer (see Fig. 5), the intensity is reduced by resonant absorption and non-resonant absorption. The resonant absorption also depends on the γ-ray energy according to the Lorentzian function. In the embedded layer dt, the γ-rays are resonant-scattered by the nuclear resonance, and also non-resonant-scattered by Rayleigh scattering recoillessly and non-recoillessly and by Compton scattering non-recoillessly. In those resonant-scattered γ-rays, f_1 portion of them are recoillessly scattered, $(1 - f_1)$ portion of them are non-recoilessly scattered. As the scattered γ-rays are coming out of the scatterer, recoillessly scattered γ-rays are subjected to both resonant absorption and non-resonant absorption, while non-recoilless scattered γ-rays are subjected to non-resonant absorption only. The γ-ray detector counts all γ-rays with energy around 14.4 kev, so integration over the incident γ-ray energy is required to get a total detector count.

Computation of scattering of non-recoilless incident γ-rays is simple; since they are only non-resonantly absorbed and scattered, there is no energy distribution complexity involved.

The total detector count depends on the Doppler velocity. As explained in the background section, E_0 is usually slightly different from E_1. Therefore the energy distribution of incident recoilless γ-rays does not fully overlap with the energy distribution of resonant absorption by the scatterer. The Doppler velocity shifts the incident γ-ray energy distribution, so that for some v, the two distributions coincide (resonance occurs), while for other v, the two distributions are fully split (off-resonance).

The detailed derivations of the mathematical expressions for the seven contributions were provided in ref.23 and are provided here in Appendix 1.

3.1.2. Why Non-Monotonic Saturation ?

The formulae in Table 1 may be used for many applications, e.g. curve fitting and peak shape analysis. One of the important applications is relating the peak amplitude, or area underneath the peak to the specimen thickness, or amount of material that contributes to that peak.

Intuitively one would expect that the peak amplitude of the BMS would increase linearly with the scatterer thickness for thin scatters, then begin to level off as the thickness increases further, and finally would saturate to a certain value. Indeed, this is how the transmission Mössbauer spectrum behaves [ref.3-9]. But actually if the numerical calculation of the peak amplitude vs scatterer thickness is plotted based on the formulas in Table 1, it shows non-monotonic saturation as plotted in Figures 1 and 2. Why does non-monotonic saturation occur?

The peak amplitude of BMS is defined as $N(0) - N(\infty)$, i.e. the γ-ray count at resonant velocity minus the count at off-resonant velocity. From Table 1 it can be seen that the contributions (6) and (7) are independent of Doppler velocity, so they are irrelevant to the peak amplitude.

The sum of the other five contributions at resonant velocity (as N(0) in Figure 4) and at off-resonant velocity (as N(∞) in Figure 4) are plotted respectively as a function of scatterer thickness for stainless steel in Figure 4. It can be seen from Figure 4 that N(0) saturates at smaller thickness than N(∞) does. This makes sense because at resonant Doppler velocity, the absorption processes are resonant absorption plus non-resonant absorption, while at off-resonant Doppler velocity, there is only non-resonant absorption. The greater the absorption, the smaller the saturation thickness is. It is the difference in the saturation thickness between N(0) and N(∞) that results in the non-monotonic saturation of the peak amplitude with the scatterer thickness.

3.1.3. Criterion of negative amplitude BMS

The method of obtaining information on the specimen being studied from the BMS includes analysis of peak position and amplitude. If some phases or chemical elements show their existence via "dips" rather than peaks, the analysis becomes confusing. It is necessary to understand under what circumstances the nuisance "dip" appears. Since the conditions for the appearance of a dip are not clear from simply looking at the integration formulas in Table 1 and doing numerical calculation, a simple expression is presented here for the criterion of negative peak BMS. The criterion itself also gives insight about why negative amplitude BMS can appear.

From Table 1 it can be seen that not only the contributions from resonant scattering of recoilless incident γ-rays (types (1) and (2)) are Doppler velocity dependent, but also the contributions from non-resonant scattering of recoilless incident γ-rays (types (3), (4) and (5)) are Doppler velocity dependent. If the individual contributions to the BMS are plotted against Doppler velocity, the contributions from (1) and (2) show a peak at resonant velocity, but the contributions from (3), (4) and (5) show a dip at resonant velocity. The reason is that although the probability (expressed as cross section) of non-resonant scattering is independent of the Doppler velocity, the number of incident recoilless γ-rays

that are scattered by the non-resonant scattering does depend on the Doppler velocity: at off-resonant velocity, for a thick enough scatterer, all incident recoilless γ-rays are absorbed and scattered non-resonantly; at resonant velocity, most incident recoilless γ-rays are resonantly absorbed and scattered, leaving only a small share of incident γ-rays available to be non-resonantly absorbed and scattered.

The total BMS is obtained by adding the contributions from the various types of scattering. When the non-resonant BMS and resonant BMS curves are added, if the dip produced by non-resonant scattering of recoilless incident γ-rays exceeds the peak produced by resonant scattering of recoilless incident γ-rays, the negative amplitude BMS should appear.

As the Doppler velocity changes from non-resonance to resonance, more and more γ-rays that would have been absorbed non-resonantly will be absorbed resonantly. One resonantly absorbed γ-ray photon will re-emit a γ-ray photon with the probability of $1/(1+\alpha)$, where α is the internal conversion coefficient as explained in the background section. But if this γ-ray were absorbed non-resonantly, a γ-ray photon would be scattered with the probability of U_s / U, where U is the total non-resonant absorption coefficient that is the sum of the non-resonant scattering absorption coefficients U_s and the photoelectronic absorption coefficient U_p. Apparently if $1/(1+\alpha)$ is less than U_s / U, the γ-ray count shows a minimum at resonant velocity. So the criterion for appearence of negative amplitude BMS is:

$$1 / (1 + \alpha) < U_s / U \tag{1.a}$$

The above criterion is derived from the physical point of view of the scattering process, but it can also be derived roughly from Bara's equations listed in Table 1. All of the symbols in the following derivation have been defined in the "List of Symbols". (For simplicity the angular distribution of resonant scattering is assumed to be same as that for Compton and Rayleigh scattering.)

The integrals in Table 1 can be analytically solved for an infinitely thick scatterer as shown in the equations (8) and (9) in Table 1, then the peak amplitude can be written as:

$$N(0) - N(\infty) \sim \frac{f_1 U_r}{(1+\alpha) X_r (X_r + 1)} + \frac{(1 - f_1) U_r}{(1+\alpha) X_n (X_n + 1)} + \frac{f_R U_R}{X_r}$$

$$+ \frac{(1 - f_R) U_R}{X_n} + \frac{U_C}{X_n} - U_R - U_C$$

$$= \frac{U_r}{(1+\alpha) X_r (X_r + 1)} + \frac{(1 - f_1) U_r}{(1+\alpha)} \left[\frac{1}{X_n (X_n + 1)} - \frac{1}{X_r (X_r + 1)} \right]$$

$$+ \frac{U_R + U_C}{X_r} - U_R - U_C + (1 - f_R) U_R \left(\frac{1}{X_n} - \frac{1}{X_r} \right) + U_C \left(\frac{1}{X_n} - \frac{1}{X_r} \right)$$

The second, sixth and seventh terms are of second order with respect to the others, so the above equation becomes:

$$\approx \frac{U_r}{(1+\alpha) X_r (X_r + 1)} - (U_R + U_C) \left(1 - \frac{1}{X_r} \right)$$

$$\sim \frac{U_r}{(1+\alpha)(X_r^2 - 1)} - (U_R + U_C)$$

$$= \frac{U_r U}{(1+\alpha) U_r} - (U_R + U_C)$$

$$\sim \frac{1}{1+\alpha} - \frac{U_R + U_C}{U}$$

$$= \frac{1}{1+\alpha} - \frac{U_s}{U} \qquad (1.b)$$

If the first term is less than the second term, N(0) is less than N(∞).

3.2. Analysis of conversion x-ray BMS

The mathematical description for x-ray BMS has not been fully studied so far. Very few previous works can be found [ref.25].

The consideration here of the x-ray BMS is somewhat accidental. The purpose of our initial experiments was to verify Bara's prediction of non-monotonic saturation of peak amplitude of γ-ray BMS with the scatterer thickness. After collecting a series of BMS on Fe specimens with a range of thicknesses, we realized that the spectra we had collected were conversion x-ray BMS rather than γ-ray BMS. However, it was interesting to observe that the results of conversion x-ray BMS also showed non-monotonic saturation of peak amplitude vs. scatterer thickness. Bearing in mind the similarities and differences between the γ-ray BMS and x-ray BMS, we modified Bara's theory of γ-ray BMS to conversion x-ray BMS and derived mathematical expressions for x-ray BMS that explained our experimental results very well.

In the analysis, the incident radiations that should be considered are 14.4 keV recoilless γ-rays, 14.4 keV non-recoilless γ-rays, and 6.4 keV x-rays. Other high energy γ-rays (122 keV, 136 keV) can be neglected. In order to measure the conversion x-ray BMS, the energy window of the backscattering detector is set around 6.4 keV to only allow photons with that energy to be counted.

The photons being counted by the x-ray detector result from four physical processes:

(a) The recoilless incident γ-rays are resonantly absorbed, and excite the ^{57}Fe in the scatterer. The de-excitation of the ^{57}Fe is via two paths, by re-emitting γ-rays or by transferring the de-excitation energy to inner shell electrons (K-shell electrons). In the latter case, the K-shell electron is ionized after receiving that energy, leaving a vacancy in that shell. An electron in an outer shell then jumps to that vacancy, releasing the energy difference between the two shells either by radiating x-rays (L-shell to K-shell jumping emits Kα x-ray of 6.398 keV energy for Fe), or ionizing another electron (so called Auger electron). The ratio of the probability of emitting a x-ray to the probability of ejecting an Auger electron is expressed as the x-ray fluorescent yield coefficient, which are listed for various elements in ref. 32.

(b) The recoilless incident γ-rays ionize the K-shell electrons directly, and Kα fluorescent x-rays are emitted.

(c) The non-recoilless part of incident γ-rays ionize the K-shell electrons, and Kα fluorescent x-rays are emitted.

(d) The 6.4 kev incident x-rays are non-resonantly scattered (Rayleigh and Compton scattering).

All four processes produce 6.4 kev radiations. The mathematical expressions for the four processes are derived as follows with the aid of Figure 6. (Definitions will be provided for all symbols not defined in the " List of Symbols " .)

The incident recoilless γ-rays with energy between E and E+dE have intensity I_0 (E,V),

$$I_0(E, V) = I_0 f_0 \frac{(\Gamma/2)^2}{(\Gamma/2)^2 + (E - E_0 - V)^2} \frac{2}{\pi\Gamma} dE \tag{2}$$

where the normalized Lorentzian function is defined as:

$$L(E) = \frac{(\Gamma/2)^2}{(\Gamma/2)^2 + (E - E_0 - V)^2} \frac{2}{\pi\Gamma} \tag{2.1}$$

$I_0(E, V)$ is reduced as it enters the scatterer by non-resonant absorption and resonant absorption. The resonant absorption depends on the incident γ-ray energy according to the Lorentzian function. Let $I_1(E, V)$ stand for the γ-ray intensity at depth t,

$$I_1(E, V) = I_0(E, V) \exp[- (U_r \frac{(\Gamma/2)^2}{(\Gamma/2)^2 + (E - E_1)^2} + U) t \operatorname{cosec} \beta_1] \, dE \tag{3}$$

After this initial penetration, the reduced intensity $I_1(E, V)$ reacts with the material in the dt layer through two ways: either γ-rays are resonantly absorbed, and then produce the conversion x-rays; or non-resonantly absorbed, and then induce x-ray fluorescence. If $I_2r(E, V)$ is the number of x-rays reacting the first way, and $I_2n(E, V)$ the second way,

$$I_2r(E, V) = I_1(E,V) U_r \frac{(\Gamma/2)^2}{(\Gamma/2)^2 + (E - E_1)^2} \frac{\alpha f_y}{1 + \alpha} dt \operatorname{cosec} \beta_1 \tag{4}$$

$$I_2n(E, V) = I_1(E, V) U_p f_y \, dt \operatorname{cosec} \beta_2 \tag{5}$$

As I_2n and I_2r come out of the scatterer, they are subjected to photoelectronic absorption, (but the absorption coefficient here is for wavelength of 1.982 (6.4 keV)).

Integrating over E and t gives the total number of conversion x-rays $N_r(S_0)$, and the total number of fluorescent x-rays $N_n(S_0)$, produced by recoilless incident γ-rays. To simplify the expressions, substitute $y = 2(E - E_0)/\Gamma$, $S_0 = 2V/\Gamma$, $S_1 = 2(E_1 - E_0)$, $T = (U_1 \operatorname{cosec} \beta_1 + U_2 \operatorname{cosec} \beta_2) t_0$. The final expressions are

$$N_r(S_0) = \frac{f_0 I_0 U_r \operatorname{cosec}\beta_1 \alpha f_y}{\pi(1+\alpha)(U_1 \operatorname{cosec}\beta_1 + U_2 \operatorname{cosec}\beta_2)} \int_{-\infty}^{\infty} dy\, Z_{x_n}(y, S_0) \tag{6}$$

$$N_n(S_0) = \frac{f_0 I_0 U_p f_y \operatorname{cosec}\beta_1}{\pi(U_1 \operatorname{cosec}\beta_1 + U_2 \operatorname{cosec}\beta_2)} \int_{-\infty}^{\infty} dy\, [(y - S_0)^2 + 1]\, Z_{x_n}(y, S_0) \tag{7}$$

with

$$Z_{x_n}(y, S_0) = \frac{1 - \exp\left[-T \dfrac{(y - S_1)^2 + x_n^2}{(y - S_1)^2 + 1}\right]}{[(y - S_0)^2 + 1][(y - S_1)^2 + x_n^2]} \tag{8}$$

$$x_n^2 = 1 + U_r \operatorname{cosec}\beta_1 / (U_1 \operatorname{cosec}\beta_1 + U_2 \operatorname{cosec}\beta_2) \tag{9}$$

U_1 and U_2 are the photoelectronic absorption coefficients for radiation energies of 14.4 kev and 6.4 keV, and f_y is the fluorescent yield coefficient.

The expression N_f for contribution (c) is easy to obtain. The incident non-recoilless γ-rays have intensity of $I_0(1 - f_1)$; when multiplied by $U_p f_y$, this gives the x-rays fluorescence produced. Integrating over the specimen thickness, t_0, gives

$$N_f = \frac{I_0(1 - f_0) U_p f_y \operatorname{cosec}\beta_1}{U_1 \operatorname{cosec}\beta_1 + U_2 \operatorname{cosec}\beta_2} [1 - \exp(-T)] \tag{10}$$

If the incident x-ray intensity is αf_y times the incident γ-ray intensity I_0, the expression for the contribution (d) is

$$N_{R+C} = \frac{I_0 \alpha f_y (U_C + U_R)}{U_2(\operatorname{cosec}\beta_1 + \operatorname{cosec}\beta_2)} [1 - \exp(-U_2 t_0 (\operatorname{cosec}\beta_1 + \operatorname{cosec}\beta_2))]$$

(11)

The equations (6) (7) (10) and (11) are listed in Table 2 to compare with J. J. Bara's equations in Table 1.

Equations (6) (7) (10) and (11) have many useful applications. For example, the numerical calculation of peak amplitude of conversion x-ray BMS vs. scatterer thickness of pure Fe is plotted in Figure 4. Apparently similar to the behavior of peak amplitude of γ-ray BMS vs. scatterer thickness, the peak amplitude of conversion x-rays BMS shows non-monotonic saturation with scatterer thickness.

The high energy γ-rays (122 keV and 136keV) are not included in the calculation for two reasons: the non-resonant absorption coefficients of them are much smaller than that of 14.4 keV; even if they are taken into consideration, the fluorescent x-rays induced by them are doppler velocity independent, so that they are not relevant to the peak amplitude $N(0) - N(\infty)$.

Another interesting concomitant result of the above theory is the criterion of negative amplitude x-ray BMS:

$$\alpha / (1 + \alpha) < U_p / U \qquad (12)$$

Its interesting implication will be discussed later.

4. EXPERIMENTS

The experiments were conducted with two purposes in mind: (1) to test Bara-Jaggi's theory of γ-ray BMS for a scatterer of finite thickness, and in particular to investigate the possible appearance of negative amplitude BMS, and (2) to test the computation of x-ray BMS by checking whether or not the peak amplitude of x-ray BMS saturates non-monotonically with the scatterer thickness.

4.1. γ-ray BMS of Be containing Fe impurities

4.1.1. Choosing materials

In section 3.1.3. a criterion for negative amplitude BMS was developed. The question addressed here is what materials satisfy the criterion.

For ^{57}Fe, the internal conversion coefficient α is fixed and equal to 8.21. But the non-resonant scattering coefficient U_s and non-resonant absorption coefficient U ($U = U_s + U_p$) depend on the matrix material in which ^{57}Fe is located.

Generally speaking, both U_s and U_p increase with the atomic number Z, but U_p increases more. Therefore the ratio of U_s/U is relatively large for light Z elements. Table 4 lists the U_s /U for the elements Li, Be, C, etc. in the order of the periodic table. The U_s /U values in Table 4 are not guaranteed to be accurate, because although experimental values for U can be found [ref.19], U_s cannot. The U_s values in Table 4 were calculated as follows.

To find the Rayleigh scattering coefficient, the formula on page 159 of ref. 26 was used:

$$\frac{d[\sigma_{coh}/\rho]}{d\Omega} = \frac{N}{A}\frac{e^4}{m^2c^4}\frac{1+\cos^2 2\theta}{2} f^2[\sin\theta/\lambda] \tag{13}$$

where σ_{coh} / ρ is the mass coefficient for coherent scattering, Ω is the solid angle, N is Avogadro's constant, A is the atomic weight, e and m are charge and mass for a rest electron, 2θ is the angle between the incident and backscattering rays, and f is the atomic scattering factor (table 3.3.1A lists f as function of $\sin\theta/\lambda$). The Rayleigh scattering coefficient U_R/ρ is calculated as:

$$U_R / \rho = \int_0^{\infty} \frac{d[\sigma_{coh} / \rho]}{d\Omega} d\Omega \tag{14}$$

For calculation of the Compton scattering coefficient, the list of ϕ_{inc}/R in Table 3.4.4.2A in ref. 26 was used, where ϕ_{inc} is defined as I_{inc} / I_e, incoherent scattering intensity expressed in the scale of scattering intensity of one electron. I_e is calculated from formulas in ref. 27.

From Table 4 it can be seen that if Fe atoms (or impurities) are embedded in a matrix of Li, Be, and C, negative amplitude BMS may appear. The matrix material Be with Fe impurity was chosen for this study because Fe is a natural impurity in Be, and Be is easy to obtain in a Mössbauer spectroscope laboratory.

As expressed in Formula (12), the criterion for negative amplitude x-ray BMS is $\alpha / (1 + \alpha) < U_p / U$, so the negative amplitude x-ray BMS is most likely to occur for Fe embedding in heavy element matrix.

4.1.2. Mössbauer Spectroscope Apparatus

All Mössbauer spectra were obtained in backscatter geometry with an Austin Science Associates S-600 constant acceleration spectrometer. All spectra were obtained with the source and absorber at room temperature. The radiation source was ^{57}Co in Rh with the intensity of 23.4 mCi. The backscatter photon detector was of toroidal geometry with high geometrical collection efficiency [ref.29]. The incident radiation passed through the hole in the torous, and backscattered radiations entered the detector through its large

toroidal window. For good efficiency for counting 14.4 keV γ-rays the detector was filled with a mix of 47 % Kr, 47 % Ar, and 6 % methane gas [ref. 30]. The voltage applied to the gas detector was 1700 V. The Mössbauer spectrometer system was explained in ref.28.

4.1.3. Specimens

Slab pieces of Be metal with a thickness of 7 mm were combined and stacked to obtain specimens with thicknesses of 7 mm, 14 mm, 21 mm, 28 mm, and 35 mm. The chemical composition of the specimen as listed by the manufacturer is shown in Table 6.

4.2. Conversion x-ray BMS of Pure Fe

4.2.1. Specimens

For the experimental measurements Fe of purity 99.999 % was used. The Fe was rolled into foils; foil thicknesses were measured by weighing method. To make specimens with a series of thicknesses, thin foils were added and stacked.

4.2.2. Experimental Parameters

A flowing gas of 90% Ar plus 10% methane was used in the backscatter gas detector. The applied voltage was 1700 V.

5. RESULTS AND DISCUSSION

5.1 γ-ray BMS Results

The backscattering Mössbauer spectra of Be metal for the specimen thicknesses of 7 mm, 14 mm, and 35 mm are plotted in Figure 7. There is a peak to dip transition as the specimen thickness increases. Figures 8 and 9 show the PHA (pulse height analysis) of the backscattered γ-rays by the 7 mm and 35 mm Be specimen.

The peak height vs specimen thickness relationship for Be with 0.1 % weight percent of Fe impurity was numerically calculated and plotted in Fig.10. The program used for calculation is listed in Table 3.

A similar experiment was reported by J. J. Bara [ref.31].

5.2 x-ray BMS Results

The peak amplitude of conversion x-ray BMS vs specimen thickness relation was numerically calculated and is plotted in figure 11. The peak amplitude should saturate non-monotonically with specimen thickness if the theory is correct.

The conversion x-ray BMS of Fe for specimens with a series of thickness are plotted in Figures 12-18. The peak amplitudes were simply measured by a ruler; no fitting program was used.

Since the absolute value of the peak amplitude is proportional to the time spent in collecting the BMS, the peak amplitudes for each spectrum were normalized into the amplitude per unit collecting time. Another necessary correction to the peak amplitude involves taking into account the decaying γ-ray source intensity. The half life of the γ-ray source is 270 days; i.e. the intensity I(t) at any time t (in the unit of day) is:

$$I(t) = I_0 \exp[-(t/270)\ln 2] \qquad (15)$$

where I_0 is the intensity at time zero. Thus one hour of collecting time at I_0 is not equivalent to one hour of collecting time at I(t). The effective collecting time Δt_e is defined as the equivalent collecting time at I_0, and is expressed as

$$\Delta t_e = \int_0^{\Delta t} dx \exp[\frac{\ln 2}{270} (t + x)] \tag{16}$$

where Δt is the collecting time for the spectrum of interest, and t is the time at which the collection started. In Figures 12-18 the peak amplitudes were normalized to the same effective collecting time. All the information, including specimen thickness, above mentioned t, Δt, and Δt_e, count at resonance and off-resonance, peak amplitude, etc. have been summarized in Table 5.

Since the Fe spectrum is a symmetrical sextet, peaks 1 and 6 were summed and averaged as the peak 1 amplitude; this was also done for the peaks 2 and 5 pair, and the peaks 3 and 4 pair. The amplitudes of peaks 1, 2, and 3 vs. specimen thickness are plotted in Figures 19-21. The data exhibit non-monotonic saturation.

5.3 Comparison of Theory with Experimental Results

5.3.1 γ-ray BMS

Comparing Figure 7 with Figure 10, the transition thickness from peak to dip is 1.1 cm predicted by the numerical calculation (see Figure 10), this value is close to the 1.4 cm from the experimental data (see Figure 7).

5.3.2 x-ray BMS

Comparing Figure 11 with Figure 19, the maximum amplitude thickness predicted by the numerical calculation is about 0.35 mils (see Figure 11). This value is close to the 0.5 mils from the experimental data (see Figure 19).

6. CONCLUSION

(1) Based on the Bara-Jaggi's mathematical theory of γ-ray backscattering Mössbauer spectrum for finite thickness specimen, the criterion for occurrence of negative amplitude Mössbauer spectrum is derived as $1 / (1 + \alpha)$ less than U_S / U. This implies that negative amplitude Mössbauer spectrum is very much more likely to occur for the case when the Mössbauer elements are in the matrix materials with very low atomic number Z (Li, Be, and C).

(2) The backscattering Mössbauer spectra collected on the Be specimen with Fe impurity proves the existence of negative amplitude Mössbauer spectrum.

(3) Parallel to Bara-Jaggi's theory, a new mathematical theory on the conversion x-ray Mössbauer spectrum has been derived. The numerical calculation based on that theory predicts a non-monotonic saturation of the peak amplitude of conversion x-ray backscattering Mössbauer spectrum with specimen thickness, just as Bara-Jaggi's theory did for the γ-ray Mössbauer spectrum.

(4) The conversion Mössbauer spectra collected on Fe for the specimens with a range of thickness showed that the peak amplitude saturated with the specimen thickness non-monotonically.

REFERENCE

[1] B. Fultz, Ph.D thesis, University of California, Berkeley (1982) LBL-13588.

[2] N. K. Jaggi, Ph.D thesis, University of Bombay, Trombay (1982).

[3] S. Margulies and J. R. Ehrman, Nuclear Instruments and Methods 12 (1961) 131.

[4] N. N. Delyagin, V. S. Shpinel, and V. A. Bryukhanov, Soviet Physics JETP, 14 (1962) 959.

[5] S. L. Ruby and J. M. Hicks, Rev. Sci. Instr. 23 (1962) 27.

[6] S. Margulies, P. Debrunner and H. Frauenfelder, Nuclear Instruments and Methods 21 (1963) 217.

[7] G. A. Bukov and Pham Zuy Hien, Soviet Physics JETP 16 (1963) 646.

[8] J. Heberle, Nuclear Instruments and Methods 58 (1968) 90.

[9] R. E. Meads, B. M. Place, F. W. D. Woodhams, and R. C. Clark, Nuclear Instruments and Methods 98 (1972) 29.

[10] N. Hershkowitz, R. D. Ruth, S. A. Wender and A. B. Carpenter, Nuclear Instruments and Methods 102 (1972) 205.

[11]. S. A. Werder, and N. Hershkowitz, Nuclear Instrument and Methods 98 (1972) 105.

[12] A. J. Stone, Nuclear Instruments and Methods 107 (1973) 285.

[13] G. Hembree and D. C. Price, Nuclear Instruments and Methods 108 (1973) 99.

[14] G. K. Shenoy and J. M. Friedt, Nuclear Instruments and Methods 116 (1974) 573.

[15] G. Dehe, B. Seidel, and W. Meisel, Nuclear Instruments and Methods 133 (1976) 381.

[16] G. J. Long, T. E. Cranshaw, and G. Longworth, Mössbauer Effect Reference and Data Journal 6 (1983) 42.

[17] Mössbauer Spectroscopy Applied to Inorganic Chemistry vol. 1, eds Gary J. Long, Plenum Press, New York and London (1984).

[18] V. G. Bhide, Mössbauer Effect & its Application, Tata McGraw-Hill Publishing Co. LTD, New Delhi (1973)

[19] P. Debrunner and R. J. Morrison, Review of Scientific Instruments 36 (1965) 145.

[20] B. Balko and G. R. Hoy, Physical Review B10 (1974) 4523.

[21] J. J. Bara and B. F. Bogacz, Phys. Stat. Sol. A44 (1977) k107.

[22] J. J. Bara and B. F. Bogacz, Mössbauer Effect Reference & Data Journal 3 (1981) 217.

[23] J. J. Bara, Phys. Sta. Sol. A58 (1980) 349.

[24] G. Breit and E. P. Wigner, Phys. Rev. 49 (1936) 904.

[25] H. K. Chow, R. F. Weise, and P. Flinn, Mössbauer Effect Spectrometer for Analysis of Iron Compounds special report NSEC-4023, contract No. At-(30-1)-4023, Chapter 3. [26] International Table on x-ray Crystallography, v.3

[27] Handbook of Physics, eds E. U. Condon and Hugh Odishaw, McGraw-Hill Book Company, Inc. New York Toronto London,p.7-128,

[28] B. Fultz, Rev. Sci. Instrum, 49 (1978) 1216

[29] B. Fultz, United States Patent 4,393,306 Jul. 12, 1983

[30] B. Fultz, private communication.

[31] J. J. Bara, J. de physique, vol 41, c1, (1980) p.13

[32] L. S. Birks, x-ray Spectrochemical Analysis, 2nd edition, Interscience Publishers, New York / London / Sydney / Toronto (1969), Appendix 3.

Appendix 1

Detailed derivation of the equation (1) - (7) listed in Table 1

(with reference to Figure 5, Reference 23, and "List of Symbols")

There are two kinds of 14.4 keV γ-rays from a γ-ray source, recoillessly emitted and non-recoillessly emitted γ-rays.

The recoillessly emitted γ-rays are absorbed by resonant absorption (Mössbauer effect absorption), and non-resonant absorption - they are Rayleigh scattering absorption and Compton scattering absorption. The Rayleigh scattering can be of recoilless and non-recoilless; the Compton scattering can be of non-recoilless only.

The recoillessly emitted γ-rays from the source can excite ^{57}Fe in a scatterer, and re-emit the γ-rays. Both recoillessly and non-recoillessly emitted γ-ray from the source are scattered by Rayleigh and Compton scatterings.

As the scattered γ-rays coming out, recoilllessly scattered γ-rays are absorbed by the resonant absorption and non-resonant absorption, but non-recoillessly scattered γ-rays are absorbed by non-resonant absorption only.

In summary, there are seven contributions to the γ-rays detected by a detector. They are (1) the recoillessly emitted γ-rays being resonant-scattered recoillessly and (2) non-recoillessly, (3) the recoillessly emitted γ-rays being Rayleigh scattered recoillessly and (4) non-recoillessly, (5) the recoillessly emitted γ-rays being scattered by Compton scattering, (6) the non-recoillessly emitted γ-rays being scattered by Rayleigh scattering and (7) Compton scattering. Followings are step by step derivations--

The recoilless emitted γ-rays from the source has the energy distribution of Lorentzian form:

$$I_{1r}(E, V) = I_0 f_0 \frac{(\Gamma/2)^2}{[E - (E_0 + V)]^2 + (\Gamma/2)^2} \frac{2}{\Gamma \pi} \qquad (1)$$

The non-recoilless emitted γ-rays from the source has no relevant energy distribution, its intensity is:

$$I_{1n} = I_0(1 - f_0) \qquad (2)$$

$I_{1r}(E, V)$ are absorbed as they enter the scatterer in the depth t:

$$I_{2r}(E, V) = I_{1r}(E, V) \exp[-(U_r(E, E_1) + U) \operatorname{cosec}\beta_1 t] \qquad (3)$$

where $U_r(E, E_1)$ is resonant absorption coefficient with Lorentzian distribution:

$$U_r(E, E_1) = U_r \frac{(\Gamma/2)^2}{(E - E_1)^2 + (\Gamma/2)^2} \qquad (4)$$

$I_{2r}(E, V)$ are scattered in the embedded layer dt (see Figure 5), by five different processes. Let I_{3rr}, I_{3rn}, I_{3Rr}, I_{3Rn}, and I_{Cn} represent the intensity of the γ-rays being resonant-scattered recoillessly, being resonant-scattered non-recoillessly, being Rayleigh-scattered recoillessly, being Rayleigh-scattered non-recoillessly, and being Compton-scattered non-recoillessly, then they can be expressed:

$$I_{3rr}(E, V) = I_{2r}(E, V)\, U_r(E, E_1) \frac{f_1}{(1 + \alpha)} \operatorname{cosec}\beta_1\, dt \qquad (5)$$

$$I_{3rn}(E, V) = I_{2r}(E, V)\, U_r(E, E_1) \frac{(1 - f_1)}{(1 + \alpha)} \operatorname{cosec}\beta_1\, dt \qquad (6)$$

$$I_{3Rr}(E, V) = I_{2r}(E, V)\, U_R\, f_R \operatorname{cosec}\beta_1\, dt \qquad (7)$$

$$I_{3Rn}(E, V) = I_{2r}(E, V)\, U_R\, (1 - f_R) \operatorname{cosec}\beta_1\, dt \qquad (8)$$

$$I_{3Cn}(E, V) = I_{2r}(E, V)\, U_C \operatorname{cosec}\beta_1\, dt \qquad (9)$$

As I_{3rr}, I_{3rn}, I_{3Rr}, I_{3Rn}, and I_{Cn} coming out, they are absorbed:

$$I_{4rr}(E, V) = I_{3rr}(E, V) \exp[-(U_r(E, E_1) + U) \operatorname{cosec}\beta_2 t] \qquad (10)$$

$$I_{4rn}(E, V) = I_{3rn}(E, V) \exp[-U \operatorname{cosec}\beta_2 t] \qquad (11)$$

$$I_{4Rr} = I_{3Rr}(E, V) \exp[-(U_r(E, E_1) + U) \operatorname{cosec}\beta_2 t] \qquad (12)$$

$$I_{4Rn}(E, V) = I_{3Rn}(E, V) \exp[-U \operatorname{cosce}\beta_2 t] \qquad (13)$$

$$I_{4Cn}(E, V) = I_{3Cn}(E, V) \exp[-U \operatorname{cosec}\beta_2 t] \qquad (14)$$

Rewrite above five equations after substitution:

$$I_{4rr}(E, V) = I_0 f_0 U_r \frac{f_1}{1+\alpha} \frac{(\Gamma/2)^2}{[E-(E_0+V)]^2+(\Gamma/2)^2} \frac{2}{\pi\Gamma} \operatorname{cosec}\beta_1 \, dt$$

$$\exp[-(U_r \frac{(\Gamma/2)^2}{(\Gamma/2)^2+(E-E_1)^2} + U)(\operatorname{cosec}\beta_1 + \operatorname{cosce}\beta_2) t] \qquad (10.a)$$

$$I_{4rn}(E, V) = I_0 f_0 U_r \frac{1-f_1}{1+\alpha} \frac{(\Gamma/2)^2}{[E-(E_0+V)]^2+(\Gamma/2)^2} \frac{2}{\pi\Gamma} \operatorname{cosec}\beta_1 \, dt$$

$$\exp[-(U_r \frac{(\Gamma/2)^2}{(\Gamma/2)^2+(E-E_1)^2} + U) \operatorname{cosec}\beta_1 t - U \operatorname{cosec}\beta_2 t] \qquad (11.a)$$

$$I_{4Rr}(E, V) = I_0 f_0 f_R U_R \frac{(\Gamma/2)^2}{[E-(E_0+V)]^2+(\Gamma/2)^2} \frac{2}{\pi\Gamma} \operatorname{cosec}\beta_1 \, dt$$

$$\exp[-(U_r \frac{(\Gamma/2)^2}{(\Gamma/2)^2+(E-E_1)^2} + U)(\operatorname{cosec}\beta_1 + \operatorname{cosec}\beta_2) t] \qquad (12.a)$$

$$I_{4Rn}(E, V) = I_0 f_0 (1-f_R) U_R \frac{(\Gamma/2)^2}{[E-(E_0+V)]^2+(\Gamma/2)^2} \frac{2}{\pi\Gamma} \operatorname{cosec}\beta_1 \, dt$$

$$\exp[-(U_r \frac{(\Gamma/2)^2}{(\Gamma/2)^2+(E-E_1)^2} + U) \operatorname{cosec}\beta_1 t - U \operatorname{cosec}\beta_2 t] \qquad (13.a)$$

$$I_{4Cn}(E, V) = I_0 f_0 U_C \frac{(\Gamma/2)^2}{[E-(E_0+V)]^2+(\Gamma/2)^2} \frac{2}{\pi\Gamma} \operatorname{cosec}\beta_1 \, dt$$

$$\exp[-(U_r \frac{(\Gamma/2)^2}{(\Gamma/2)^2+(E-E_1)^2} + U) \operatorname{cosec}\beta_1 t - U \operatorname{cosec}\beta_2 t] \qquad (14.a)$$

Integrate over the thickness t and energy E, and substitute into following equations:

$$y = 2(E - E_1)/\Gamma \qquad (15)$$

$$S_0 = 2\,V / \Gamma \qquad (16)$$

$$S_1 = 2\,(E_1 - E_0) / \Gamma \qquad (17)$$

then:

$$N_{rr}(S_0) = \int_{-\infty}^{\infty} dy \int_0^{t_0} dt \frac{I_0 f_0 U_r f_1}{\pi(1+\alpha)} \frac{1}{(y - S_0)^2 + 1} \frac{1}{(y - S_1)^2 + 1} \operatorname{cosec}\beta_1$$

$$\exp\left[-\left(\frac{U_r}{U}\frac{1}{(y - S_1)^2 + 1} + 1\right) T\right] \qquad (18)$$

$$N_{rn}(S_0) = \int_{-\infty}^{\infty} dy \int_0^{t_0} dt \frac{I_0 f_0 U_r (1 - f_1)}{\pi(1+\alpha)} \frac{1}{(y - S_0)^2 + 1} \frac{\operatorname{cosec}\beta_1}{(y - S_1)^2 + 1}$$

$$\exp\left[-\left(\frac{U_r}{U}\frac{1}{(y - S_1)^2 + 1}\frac{\operatorname{cosec}\beta_1}{\operatorname{cosec}\beta_1 + \operatorname{cosec}\beta_2} + 1\right) T\right] \qquad (19)$$

$$N_{Rr}(S_0) = \int_{-\infty}^{\infty} dy \int_0^{t_0} dt \frac{I_0 f_0 U_R f_R}{\pi} \frac{1}{(y - S_0)^2 + 1} \operatorname{cosec}\beta_1$$

$$\exp\left[-\left(\frac{U_r}{U}\frac{1}{(y - S_1)^2 + 1} + 1\right) T\right] \qquad (20)$$

$$N_{Rn}(E, V) = \int_{-\infty}^{\infty} dy \int_0^{t_0} dt \frac{I_0 f_0 U_R (1 - f_R)}{\pi} \frac{\operatorname{cosec}\beta_1}{(y - S_0)^2 + 1}$$

$$\exp\left[-\left(\frac{U_r}{U}\frac{1}{(y - S_1)^2 + 1}\frac{\operatorname{cosec}\beta_1}{\operatorname{cosec}\beta_1 + \operatorname{cosec}\beta_2} + 1\right) T\right] \qquad (21)$$

$$N_{Cn}(S_0) = \int_{-\infty}^{\infty} dy \int_0^{t_0} dt \frac{I_0 f_0 U_C}{\pi} \frac{\operatorname{cosec}\beta_1}{(y - S_0)^2 + 1}$$

$$\exp\left[-\left(\frac{U_r}{U}\frac{1}{(y - S_1) + 1}\frac{\operatorname{cosec}\beta_1}{\operatorname{cosec}\beta_1 + \operatorname{cosec}\beta_2} + 1\right) T\right] \qquad (22)$$

Define:

$$X_r^2 = 1 + \frac{U_r}{U} \qquad (23)$$

$$X_n^2 = 1 + \frac{U_r}{U}\frac{\operatorname{cosec}\beta_1}{\operatorname{cosec}\beta_1 + \operatorname{cosec}\beta_2} \qquad (24)$$

then (18)-(22) can be rewritten as:

$$N_{rr}(S_0) = \frac{f_0 f_1 I_0 U_r \operatorname{cosec}\beta_1}{\pi(1+\alpha)} \int_{-\infty}^{\infty} dy \int_0^{t_0} dt \frac{\exp\left[-T\dfrac{(y-S_1)^2 + X_r^2}{(y-S_1)^2+1}\right]}{[(y-S_0)^2+1][(y-S_1)^2+1]}$$

(18.a)

$$N_{rn}(S_0) = \frac{f_0 I_0 (1-f_1) U_r \operatorname{cosec}\beta_1}{\pi(1+\alpha)} \int_{-\infty}^{\infty} dy \int_0^{t_0} dt \frac{\exp\left[-T\dfrac{(y-S_1)^2 + X_n^2}{(y-S_1)^2+1}\right]}{[(1+(y-S_0)^2][(1+(y-S_1)^2]}$$

(19.a)

$$N_{Rr}(S_0) = \frac{f_0 I_0 (1-f_R) U_R \operatorname{cosec}\beta_1}{\pi} \int_{-\infty}^{\infty} dy \int_0^{t_0} dt \frac{\exp\left[-T\dfrac{(y-S_1)^2 + X_r^2}{(y-S_1)^2+1}\right]}{(y-S_0)^2+1}$$

(20.a)

$$N_{Rn}(S_0) = \frac{f_0 I_0 (1-f_R) U_R \operatorname{cosec}\beta_1}{\pi} \int_{-\infty}^{\infty} dy \int_0^{t_0} dt \frac{\exp\left[-T\dfrac{(y-S_1)^2 + X_n^2}{(y-S_1)^2+1}\right]}{(y-S_0)^2+1}$$

(21.a)

$$N_{Cn}(S_0) = \frac{f_0 I_0 U_C \operatorname{cosec}\beta_1}{\pi} \int_{-\infty}^{\infty} dy \int_0^{t_0} dt \; \frac{\exp\left[-T \dfrac{(y - S_1)^2 + X_n^2}{(y - S_1)^2 + 1}\right]}{(y - S_0)^2 + 1}$$

(22.a)

The integration over t can be analytically solved, then:

$$N_{rr}(S_0) = \frac{f_0 I_0 f_1 U_r \operatorname{cosec}\beta_1}{\pi (1 + \alpha) U (\operatorname{cosec}\beta_1 + \operatorname{cosec}\beta_2)} \int_{-\infty}^{\infty} dy \; \frac{1 - \exp\left[-T \dfrac{(y - S_1)^2 + X_r^2}{(y - S_1)^2 + 1}\right]}{[(y - S_0)^2 + 1]\,[(y - S_1)^2 + X_r^2]}$$

(18.b)

$$N_{rn}(S_0) = \frac{f_0 I_0 (1 - f_1) U_r \operatorname{cosec}\beta_1}{\pi (1 + \alpha) U (\operatorname{cosec}\beta_1 + \operatorname{cosec}\beta_2)} \int_{-\infty}^{\infty} dy \; \frac{1 - \exp\left[-T \dfrac{(y - S_1)^2 + X_n^2}{(y - S_1)^2 + 1}\right]}{[(y - S_0)^2 + 1]\,[(y - S_1)^2 + X_n^2]}$$

(19.b)

$$N_{Rr}(S_0) = \frac{f_0 I_0 f_R U_R \operatorname{cosec}\beta_1}{\pi U (\operatorname{cosec}\beta_1 + \operatorname{cosec}\beta_2)} \int_{-\infty}^{\infty} dy \; \frac{[(y - S_1)^2 + 1]\,\{1 - \exp[-T \dfrac{(y - S_1)^2 + X_r^2}{(y - S_1)^2 + 1}]\}}{[(y - S_0)^2 + 1]\,[(y - S_1)^2 + X_r^2]}$$

(20.b)

$$N_{Rn}(S_0) = \frac{f_0 I_0 (1 - f_R) U_R \operatorname{cosec}\beta_1}{\pi U (\operatorname{cosec}\beta_1 + \operatorname{cosec}\beta_2)} \int_{-\infty}^{\infty} dy \; \frac{[(y - S_1)^2 + 1]\,\{1 - \exp[-T \dfrac{(y - S_1)^2 + X_n^2}{(y - S_1)^2 + 1}]\}}{[(y - S_0)^2 + 1]\,[(y - S_1)^2 + X_n^2]}$$

(21.b)

$$N_{Cn}(S_0) = \frac{f_0 I_0 (1 - f_1) U_C \operatorname{cosec}\beta_1}{\pi U (\operatorname{cosec}\beta_1 + \operatorname{cosec}\beta_2)} \int_{-\infty}^{\infty} dy \frac{[(y - S_1)^2 + 1] \{1 - \exp[-T \frac{(y - S_1)^2 + X_n^2}{(y - S_1)^2 + 1}]\}}{[(y - S_0)^2 + 1][(y - S_1)^2 + X_n^2]}$$

(22.b)

then substitute

$$Z_{X_r}(y, S_0) = \frac{1 - \exp[-T \frac{(y - S_1)^2 + X_r^2}{(y - S_1)^2 + 1}]}{[(y - S_0)^2 + 1][(y - S_1)^2 + X_r^2]} \qquad (25)$$

$$Z_{X_r}(y, S_0) = \frac{1 - \exp[-T \frac{(y - S_1)^2 + X_r^2}{(y - S_1)^2 + 1}]}{[(y - S_0)^2 + 1][(y - S_1)^2 + X_r^2]} \qquad (26)$$

(18.b - 22.b) will become the same form as (1) - (5) in Table 1.

The equations (6) and (7) are straightforward, their derivations are omitted here.

LIST OF SYMBOLS

α: internal conversion constant.

BMS: backscattering Mössbauer spectroscopy or backscattering Mössbauer spectrum.

β_1: angle between incident γ–rays and scattering surface.

β_2: angle between scattered radiation and scatterer surface.

c: light speed.

Γ: Half Width at Full Height of nuclear resonance.

E: incident γ-ray energy.

E_0 and E_1: energy difference between excited and ground states of ^{57}Fe in the γ-ray source, and scatterer respectively. E_1 is also called resonant energy.

f: either atomic scattering factor, or recoilless constant.

f_0, f_1: recoilless constant of the γ-ray source, scatterer.

f_R: recoilless constant of Rayleigh scattering.

ME, MS: Mössbauer effect, Mössbauer spectrometer (Mössbauer spectroscopy).

N(0), N(∞): detect count at resonance, off-resonance.

λ: radiation wavelength.

t: depth of the specimen.

t_0: thickness of the specimen.

T: effective scatterer thickness. $T = t_0 U (\mathrm{cosec}\beta_1 + \mathrm{cosec}\beta_2$ for γ- ray BMS; $= t_0 (U_1 \mathrm{cosec}\beta_1 + U_2 \mathrm{cosec}\beta_2)$ for X-ray BMS.

TMS: transmission Mössbauer spectroscopy or transmission Mössbauer spectrum.

U_r: absorption coefficient of nuclear resonance.

U_R, U_C, U_p, and U: non-resonant absorption coefficients, specifically Rayleigh scattering absorption, Compton scattering absorption, and photoelectronic absorption. U is the sum these three absorptions.

U_1,U_2: non-resonant absorption coefficients at wavelength of 1.986 A (6.4 kev),

0.861 A.

v: Doppler velocity.

V: energy modulation due to Doppler velocity, $V = E_0 (1 + v / c)$.

Z: atomic number.

LIST OF TABLES

Table 1: mathematical expressions for the seven contributions to γ-ray backscattering Mössbauer spectrum. (from J. J. Bara, ref.23).

Table 2: mathematical expressions for the four contributions to X-ray backscattering Mössbauer spectrum.

Table 3: Computer program used in numerical calculation of peak amplitude vs specimen thickness curve.

Table 4: Us / U values for some elements.

Table 5: Summary of the experimental data of the conversion X-ray backscattering Mössbauer spectra of pure Fe.

Table 6: The chemical composition of the Be specimen listed by manufacturer.

Table 1: Integral expressions for the seven contributions to γ-ray backscattering Mössbauer spectrum.

$$N_{rr}(S_0) = \frac{f_0 f_1 I_0 U_r W_r(\theta) \operatorname{cosec} \beta_1) dw_1 dw_2}{\pi (1+\alpha) U (\operatorname{cosec} \beta_1 + \operatorname{cosec} \beta_2)} \int_{-\infty}^{\infty} dy\, Z_{x_r}(y, S_0) \tag{1}$$

$$N_{rn}(S_0) = \frac{f_0 (1 - f_1) I_0 U_r W_r(\theta) \operatorname{cosec} \beta_1 dw_1 dw_2}{\pi (1+\alpha) U (\operatorname{cosec} \beta_1 + \operatorname{cosec} \beta_2)} \int_{-\infty}^{\infty} dy\, Z_{x_n}(y, S_0) \tag{2}$$

$$N_{Rr}(S_0) = \frac{f_0 f_R(\theta) I_0 U_R(\theta) \operatorname{cosec} \beta_1 dw_1 dw_2}{\pi U (\operatorname{cosec} \beta_1 + \operatorname{cosec} \beta_2)} \int_{-\infty}^{\infty} dy\, [(y - S_1)^2 + 1]\, Z_{x_r}(y, S_0) \tag{3}$$

$$N_{Rn}(S_0) = \frac{f_0 [1 - f_R(\theta)] I_0 U_R \operatorname{cosec} \beta_1 dw_1 dw_2}{\pi U (\operatorname{cosec} \beta_1 + \operatorname{cosec} \beta_2)} \int_{-\infty}^{\infty} dy\, [(y - S_0)^2 + 1)]\, Z_{x_n}(y, S_0) \tag{4}$$

$$N_{Cn}(S_0) = \frac{f_0 I_0 U_C(\theta) \operatorname{cosec} \beta_1 dw_1 dw_2}{\pi U (\operatorname{cosec} \beta_1 + \operatorname{cosec} \beta_2)} \int_{-\infty}^{\infty} dy\, [(y - S_1)^2 + 1]\, Z_{x_n}(y, S_0) \tag{5}$$

$$N_R = \frac{(1 - f_0) I_0 U_R(\theta) \operatorname{cosec} \beta_1 dw_1 dw_2}{U (\operatorname{cosec} \beta_1 + \operatorname{cosec} \beta_2)} [1 - \exp(-T)] \tag{6}$$

$$N_C = \frac{(1 - f_0) I_0 U_R(\theta) \operatorname{cosec} \beta_1 dw_1 dw_2}{U (\operatorname{cosec} \beta_1 + \operatorname{cosec} \beta_2)} [1 - \exp(-T)] \tag{7}$$

with

$$Z_{X_r}(y, S_0) = \frac{1 - \exp\left[-T \dfrac{(y - S_1)^2 + X_r^2}{(y - S_1)^2 + 1} \right]}{[(y - S_0)^2 + 1][(y - S_0)^2 + X_r^2]}$$

$Z_{X_n}(y, S_0)$ is described by $Z_{X_r}(y, S_0)$ when X_r is replaced by X_n.

$$y = 2(E - E_o)/\Gamma$$

$$S_0 = 2 E_o v / c / \Gamma$$

$$S_1 = 2(E_1 - E_0)/\Gamma$$

$$X_r = 1 + U_r / U$$

$$X_n = 1 + U_r / U \ \mathrm{cosec}\, \beta_1 / (\mathrm{cosec}\, \beta_1 + \mathrm{cosec}\, \beta_2)$$

$$T = t\, U (\mathrm{cosec}\, \beta_1 + \mathrm{cosec}\, \beta_2)$$

when $T = \infty$, and $S_0 = S_1$ (at resonance):

$$\frac{1}{\pi} \int_{-\infty}^{\infty} dy \ Z_{X_r}(y, S_0) = \frac{1}{X_r} \qquad (8)$$

$$\frac{1}{\pi}\int_{-\infty}^{\infty} dy \; [\,(y - S_1)^2 + 1\,)\,] \; Z_{x_r}(y, S_0) = \frac{1}{x_r\,(x_r + 1)} \tag{9}$$

Table 2: Mathematical expressions for the four contributions to the conversion x-ray backscattering Mössbauer spectrum.

$$N_r(S_0) = \frac{f_0 I_0 U_r \operatorname{cosec}\beta_1 \alpha f_y}{\pi(1+\alpha)(U_1 \operatorname{cosec}\beta_1 + U_2 \operatorname{cosec}\beta_2)} \int_{-\infty}^{\infty} dy\, Z_{x_n}(y, S_0) \tag{1}$$

$$N_n(S_0) = \frac{f_0 I_0 U_p f_y \operatorname{cosec}\beta_1}{\pi(U_1 \operatorname{cosec}\beta_1 + U_2 \operatorname{cosec}\beta_2)} \int_{-\infty}^{\infty} dy\, [(y - S_0)^2 + 1]\, Z_{x_n}(y, S_0) \tag{2}$$

$$N_f = \frac{I_0 (1 - f_0) U_p f_y \operatorname{cosec}\beta_1}{U_1 \operatorname{cosec}\beta_1 + U_2 \operatorname{cosec}\beta_2} [1 - \exp(-T)] \tag{3}$$

$$N_{R+C} = \frac{I_0 \alpha f_y (U_C + U_R)}{U_2 (\operatorname{cosec}\beta_1 + \operatorname{cosec}\beta_2)} [1 - \exp(-U_2 t_0 (\operatorname{cosec}\beta_1 + \operatorname{cosec}\beta_2))] \tag{4}$$

with

$$Z_{x_n}(y, S_0) = \frac{1 - \exp\left[-T \dfrac{(y - S_1)^2 + x_n^2}{(y - S_1)^2 + 1}\right]}{[(y - S_0)^2 + 1][(y - S_1)^2 + x_n^2]}$$

$$x_n^2 = 1 + U_r \operatorname{cosec}\beta_1 / (U_1 \operatorname{cosec}\beta_1 + U_2 \operatorname{cosec}\beta_2)$$

$$T = t_0 U_2 (\operatorname{cosec}\beta_1 + \operatorname{cosec}\beta_2)$$

Table 3: Computer program used in numerical calculation of peak amplitude vs. specimen thickness curve.

```
c       NUMERICAL CALCULATION OF PEAK AMPLITUDE OF BACKSCATTER
C       MOSSBAUER SPECTRA AS FUNCTION OF SPECIMEN THICKNESS
c       BARA' EQUATIONS ARE USED. AFTER SLIGHTLY CHANGED, THIS
C       PROGRAM CAN BE USED TO CALCULATE THE PEAK AMPLITUDE VS
c       THICKNESS FOR CONVERSION X-RAY MS SPECTR
C       MEI, ZEQUN  4-24-87
        DIMENSION Gr(50),Gn(50),Rr(50),Rn(50),Cn(50)
        DIMENSION BG(50),Ti(50)
c       Gr,Gn,Rr,Rn,and Cn are counts at resonant doppler velocity
c       for the five scatter processes listed in Bara's paper.
c       BG is sum of Rr Rn and Cn count at off-resonant velocity
        data f1,Ug,UR,UC,U,a,T0/0.70,0.2069,0.111,0.254,0.8681,8.21,4.0/
c       input parameters needed for calculation, T0 is the thickness
c       range in unit of cm, other expressions are self-explained
        DATA B1,B2/0.7854,0.7854/
c       B1,B2:Angles of inc.,out.
        OPEN (unit=1,file='MSBRresult', status='new')
        B4 = 1.0 / SIN(B1)
        B5 = 1.0 / SIN(B2)
        B7 = B4 / (B4 + B5)
        A1 = f1 * Ug / (1.0 + a) * B7
        A2 = (1 - f1) * Ug / (1.0 + a) * B7
        A3 = f1 * f1 * UR * B7
        A4 = (1.0 - f1 * f1) * UR * B7
c           suppose f(Rayleigh)=f1*f1
        A5 = UC * B7
c       A1 A2,,,A5 are the constants for Gr,Gn,Rr,Rn, and Cn, common
c       factors  for A1,,,A5 have been omitted
        write (1,4)
        DO 100,I=1,50
           T=T0/50.0*FLOAT(I)
           TE=T*U*(B4+B5)
           Xr = SQRT(1.0 + Ug / U)
           Xn = SQRT(1.0 + Ug / U * B4 / (B4 + B5))
           CALL S(TE,Xr,1,Y)
           Gr(I)=Y*A1*C1
           Gr(I)=Gr(I)*100.0
           CALL S(TE,Xn,1,Y)
           Gn(I)=Y*A2*C1
           Gn(I)=Gn(I)*100.0
           CALL S(TE,Xr,2,Y)
           Rr(I)=Y*A3*C1
           Rr(I)=Rr(I)*100.0
           CALL S(TE,Xn,2,Y)
           Rn(I)=Y*A4*C1
           Rn(I)=Rn(I)*100.0
           Cn(I)=Y*A5*C1
           Cn(I)=Cn(I)*100.0
           BG(I)=(A3+A4+A5)*(1.0-EXP(-TE))*C1
           BG(I)=BG(I)*100.0
           TI(I)=Gr(I)+Gn(I)+Rr(I)+Rn(I)+Cn(I)-BG(I)
```

```
          T1=T
          write (1,5) T1,TI(I),Gr(I),Gn(I),Rr(I),Rn(I),Cn(I),BG(I)
100     CONTINUE
5       format (1x,f5.2,7(f10.6))
4       format (1x,5hT(um),4x,6hTotalI,4x,6hGr(T) ,4x,6hGn(T) ,4x,
     1     6hRr(T) ,4x,6hRn(I) ,4x,6hCn(T),4x,6hBG(T) )
        call close(1)
        STOP
        END


c       This is basically an intergation routine, since the integral
c       limits are +- infinite and dampling trend of the function
c       being integrated, sampling widthes change with the integral
c       varible
        SUBROUTINE S(T,X,L,Y)
        LOGICAL CON3
        PARAMETER (Pi=3.141593)
        F(T,X,Z)=2.0/Pi*(1.0-EXP(-T*(Z*Z+X*X)/(Z*Z+1.0)))/(Z*Z+1.0)
     1    / ( Z*Z+X*X )
        G(T,X,Z)=2.0/Pi*(1.0-EXP(-T*(Z*Z+X+X)/(Z*Z+X*X)))/(Z*Z+X*X)
        CON3=L.EQ.2
        SUM=0
        IF (CON3) GOTO 700
        DO 200 J=1,10
        H=1.0/2.0**J
        M=10-J
        N=2**J-1
            DO 400 I=0,N
            Z=H*FLOAT(I)+M
            SUM=SUM+F(T,X,Z)*H
400         CONTINUE
200     CONTINUE
        GOTO 800
700     DO 300 J=1,15
        K=J
        H=10.0/2.0**K
        M=150-J*10
        N=2**K-1
            DO 500 I=0,N
            Z=H*FLOAT(I)+M
            SUM=SUM+G(T,X,Z)*H
500         CONTINUE
300     CONTINUE
800     Y=SUM
        RETURN
        END
```

Table 4: Ratio of scattering (Rayleigh and Compton) to total absorption.

elements	Us: U(rayleigh) + U(comp) cm*cm/g	U(total abs.) cm*cm/g	Us / U
Li	0.0431 + 0.139	0.259	0.70
Be	0.0599 + 0.138	0.397	0.50
C	0.104 + 0.145	0.951	0.26
Na	0.264 + 0.125	5.48	0.071
Al	0.337 + 0.121	8.83	0.052
Fe	0.784 + 0.0983	64.7	0.01

Table 6: The chemical composition of Be specimen listed by manufacturer.

Element or Compound	Min. %	Max. %
Beryllium	98.5	
Beryllium Oxide		1.2
Aluminum		0.060
Carbon		0.100
Iron		0.100
Magnesium		0.08
Silicon		0.06
Sulfur		0.04
Uranium		0.04
Other elements, each		0.04

Table 5: Summaary of the experimental information from pure Fe X-ray BMS.
(in the table times have unit of hours, peaks have unit of counts).

thickness (mils)	0.098	0.196	0.294	0.472	0.820	1.13	2.23
thickness (g/cm *10)	0.0196	0.0392	.0588	0.0944	0.164	0.226	0.446
time start to collecting	0	45.9	95.0	140.9	189.6	239.1	308.73
collecting time	44.67	47.78	44.45	46.58	48.9	68.78	48.73
effective collecting time	44.56	47.42	43.90	45.77	47.79	66.80	47.02
background counts	143408	185665	190741	208336	227232	324417	236510
background count per effective time	3218.1	3914.9	4345.3	4551.9	4754.5	4856.7	5029.5
peak 1 count	158843	211412	217313	236574	256672	364344	264002
peak 1 count per effective time	3564.4	4457.9	4950.6	5168.9	5370.4	5454.5	5614.2
peak 2 count	155373	205686	211639	229385	248768	353362	256062
peak 2 count per effective time	3486.6	4337.1	4821.3	5011.8	5205.1	5290.1	5445.3
peak 3 count	147591	195026	201128	219613	239032	339796	247530
peak 3 count per effective time	3311.9	4112.3	4581.9	4798.3	5001.4	5087.0	5263.9
peak 1 minus background	346.4	542.9	605.3	617.0	616.0	597.7	584.6
peak 2 minus backgroud	268.5	422.2	476.1	459.9	450.6	433.3	415.8
peak 3 minus background	93.9	197.4	236.6	246.4	246.9	230.2	234.4

LIST OF FIGURES

Figure 1. Copy of Figure 1 in Jaggi's thesis.

Figure 2. Copy of Figure 2 in Jaggi's thesis.

Figure 3. Layout of Mössbauer spectrometer (transmission and backscattering)

Figure 4. Numerical calculation of N(0), N(∞), and N(0)-N(∞) of γ-ray BMS as function of stainless steel scatterer thickness.

Figure 5. Diagram used to derive the mathematical expression for γ-ray BMS.

Figure 6. Diagram used to derive the mathematical expression for conversion X-ray BMS.

Figure 7. γ-ray BMS of Be with specimen thickness of 7 mm, 14 mm, and 35 mm.

Figure 8. Pulse Height Analysis of the γ–rays backscattered by 7 mm Be.

Figure 9. Pulse Height Analysis of the γ-rays backscattered by 35 mm Be.

Figure 10. Numerical calculation of peak amplitude of γ-ray BMS vs scatterer thickness for Be with 0.1% (wt) natural Fe.

Figure 11. Numerical calculation of peak amplitude of conversion X-ray BMS vs scatterer thickness of pure Fe.

Figure 12. Conversion X-ray BMS of pure Fe with specimen thickness of 0.1 mils.

Figure 13. Conversion X-ray BMS of pure Fe with specimen thickness of 0.2 mils.

Figure 14. Conversion X-ray BMS of pure Fe with specimen thickness of 0.3 mils.

Figure 15. Conversion X-ray BMS of pure Fe with specimen thickness of 0.47 mils.

Figure 16. Conversion X-ray BMS of pure Fe with specimen thickness of 0.82 mils.

Figure 17. Conversion X-ray BMS of pure Fe with specimen thickness of 1.13 mils.

Figure 18. Conversion X-ray BMS of pure Fe with specimen thickness of 2.23 mils.

Figure 19. Plot of peak 1 amplitude of Fe conversion BMS vs specimen thickness.

Figure 20. Plot of peak 2 amplitude of Fe conversion BMS vs specimen thickness.

Figure 21. Plot of peak 3 amplitude of Fe conversion BMS vs specimen thickness.

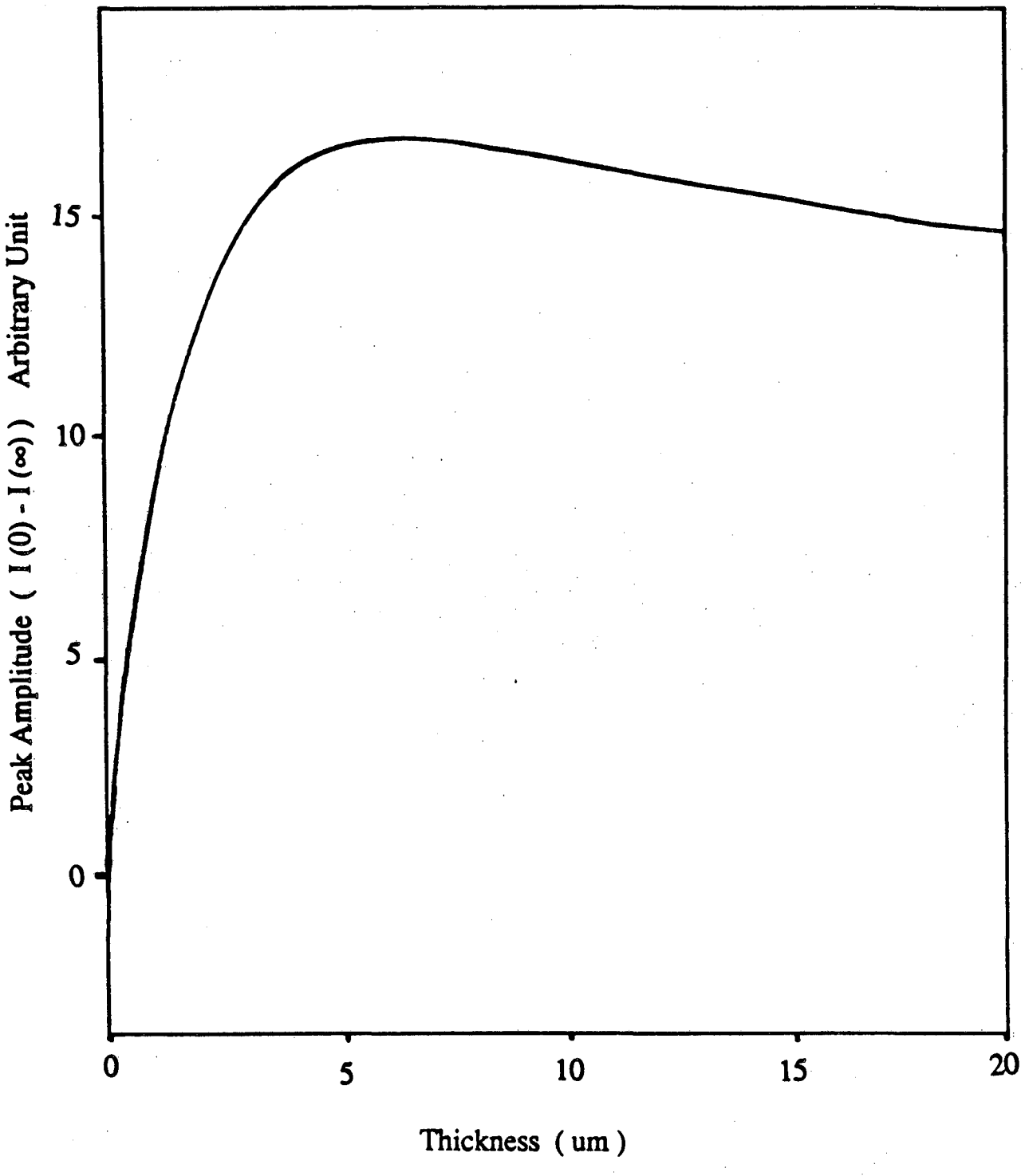

Figure1: The peak amplitudes of backscattering Mössbauer spectra vs. scatterer thickness. The material of the scatterer is stainless steel. Fe has natural abundance in the Fe. The recoilless fraction of the scatterer is 0.75, the recoilless fraction of Rayleigh scattering is 0.57. [ref. 2]

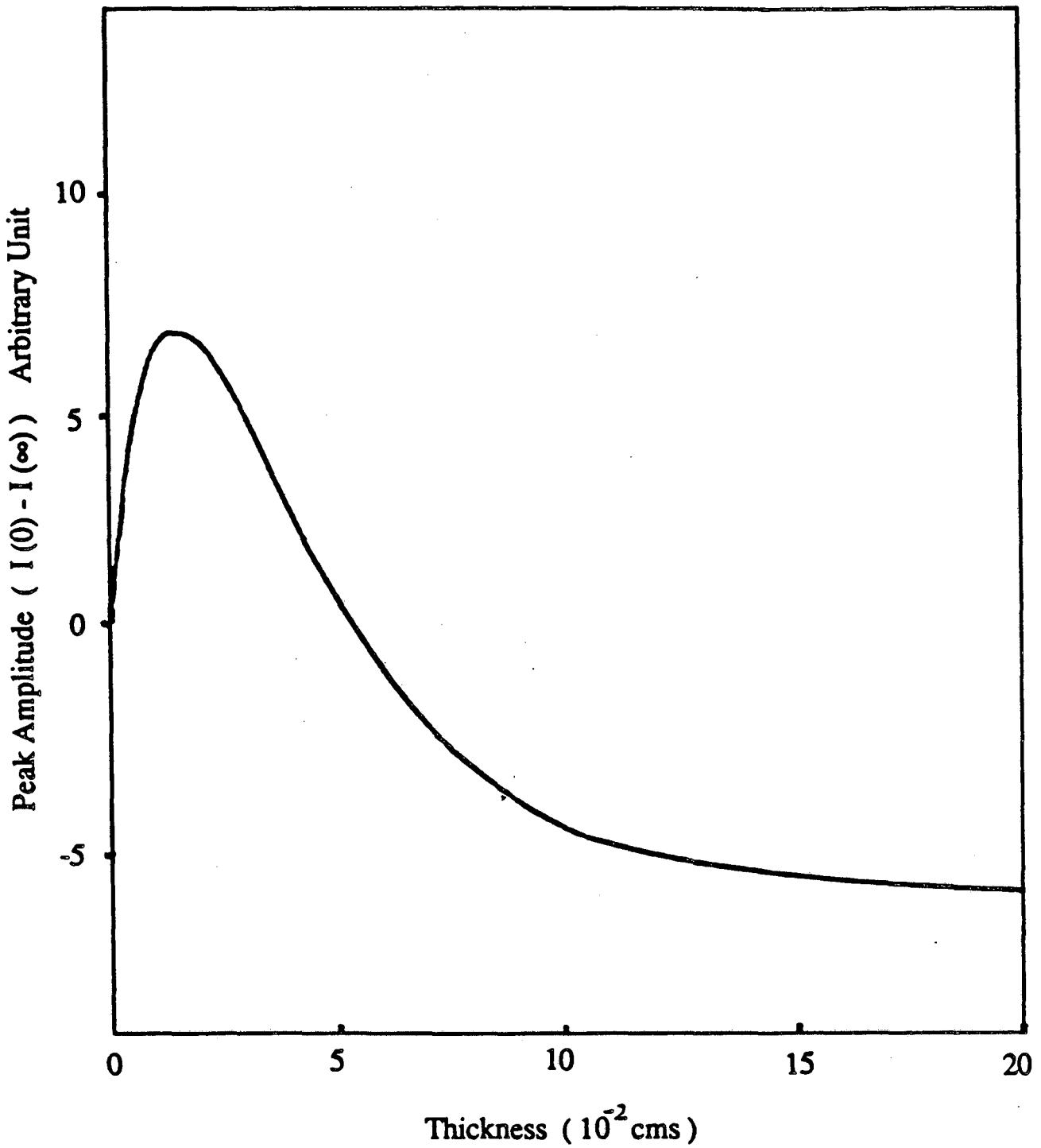

Figure 2: The peak amplitudes of backscattering Mössbauer spectra vs. scatterer thickness. The material of the scatterer is 1 wt % Fe in coal. Fe has natural abundance in the Fe. The recoilless fraction of the scatterer is 0.7, the recoilless fraction of Rayleigh scattering is 0.49. [ref. 2]

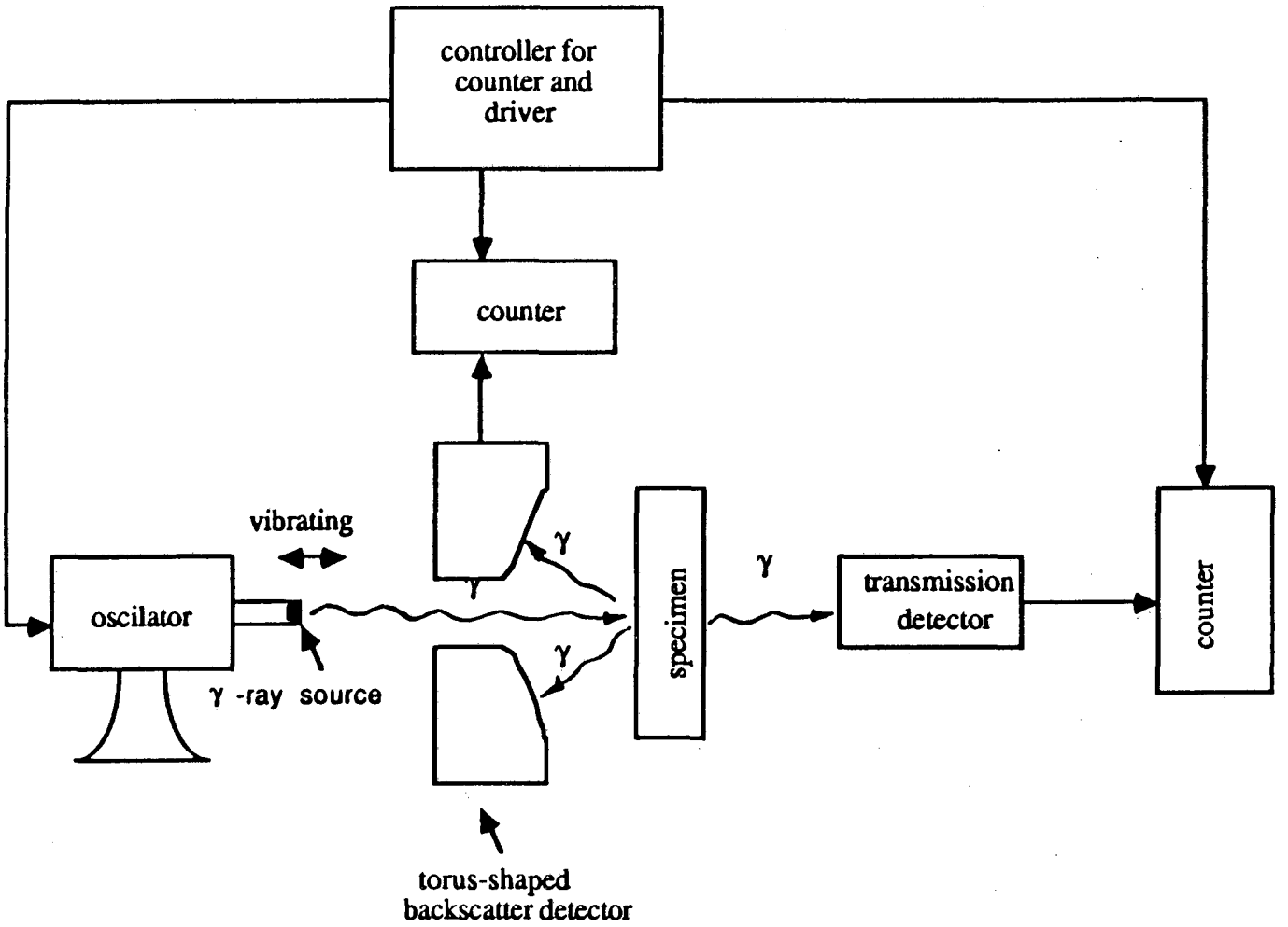

Figure 3. Layout of mössbauer spectrometer (transmission and backscattering)

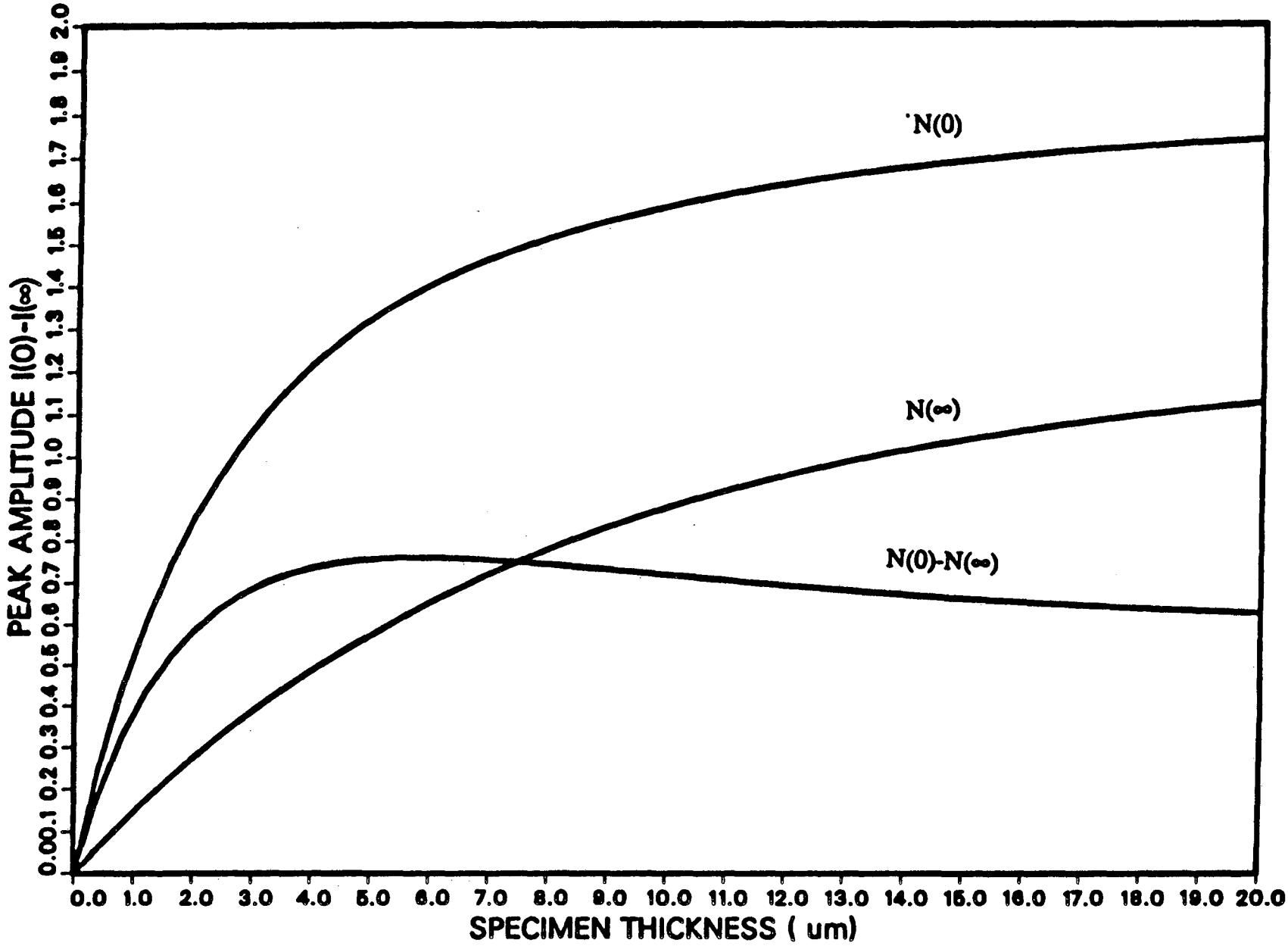

Figure 4. Numerical calculation of N(0), N(∞), and N(0) - N(∞) of γ-ray BMS as a function of stainless steel scatterer thickness.

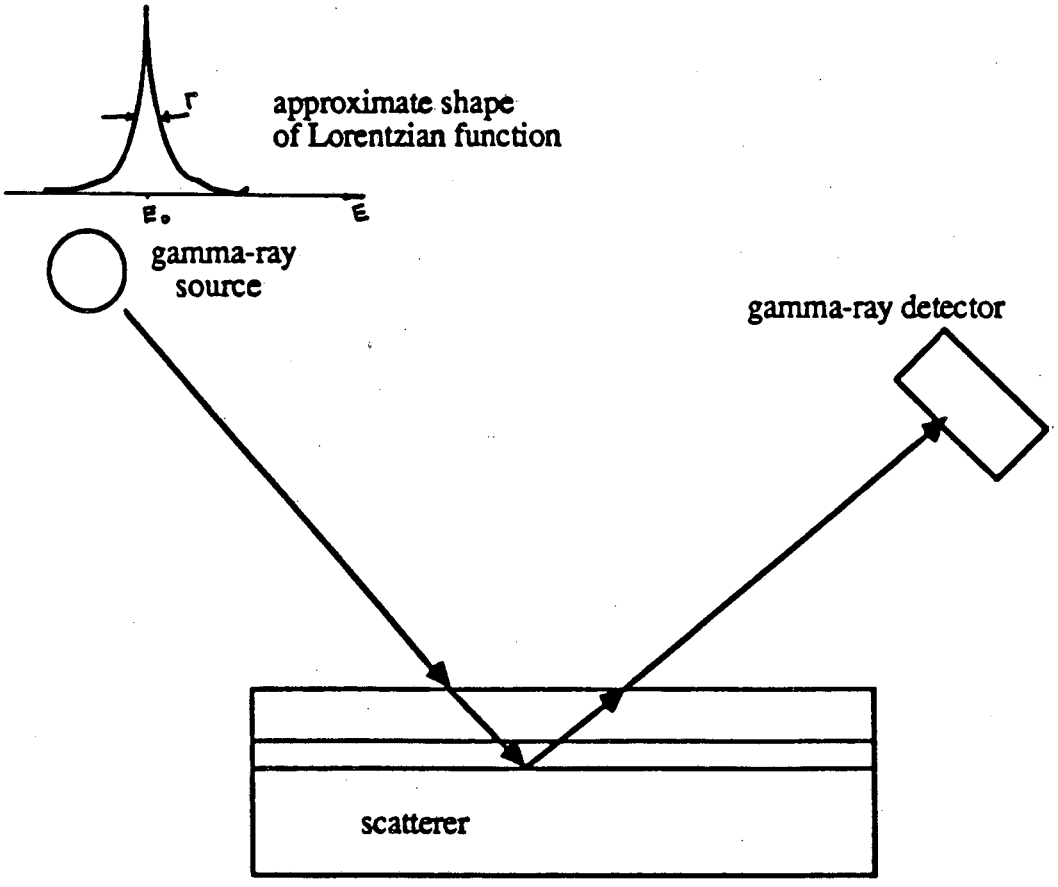

Incident radiations: (1) 14.4 keV recoilless gamma-rays

(2) 14.4 keV non-recoilless gamma-rays

(1) are either resonant-scattered recoillessly and non-recoillessly or non-resonant-scattered (by Rayleigh scattering recoillessly and non-recoillessly, or by Compton scattering non-recoillessly)

(2) are non-resonantly scattered (by Rayleigh and Compton scatterings)

Figure 5. Diagram used to derive the mathematical expressions for gamma-ray BMS

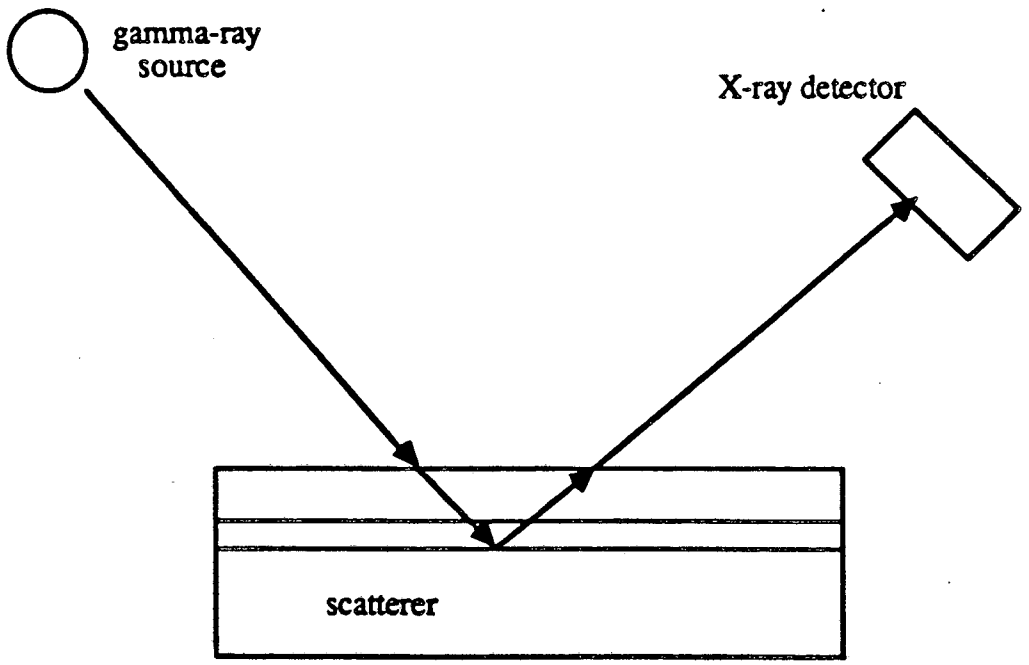

Incident radiations: (1) 14.4 keV recoilless gamma-rays

(2) 14.4 keV non-recoilless gamma-rays

(3) 6.4 keV X-rays

(1) are either resonantly absorbed and converted to 6.4 keV X-rays

or non-resonantly absorbed and excite 6.4 keV fluorescent X-rays

(2) are non-resonantly absorbed and excite 6.4 keV fluorescent X-rays

(3) are non-resonantly absorbed and scattered by Rayleigh and Compton scatterings

Figure 6. Diagram used to derive the mathematical expressions for conversion X-ray BMS

Figure 7: The Mössbauer spectra of Be specimens containing < 0.1 % Fe for the specimen thickness of 7 mm, 14 mm, and 35 mm.

TITLE FOR PLOT:	Backscatter Mossbauer Spectra of Be
X SCALE (POINTS/IN):	45
MAXIMUM VELOCITY:	2.42
ZERO VELOCITY OFFSET:	0
NO. OF FILES:	3

PLOT NO.	1	2	3
SYMBOL	+	.	o
FILE NAME	7 mm	14 mm	35 mm
BASE LINE VALUE	1045000	422848	578000
Y SCALE (COUNTS/IN)	15000	7354	10000

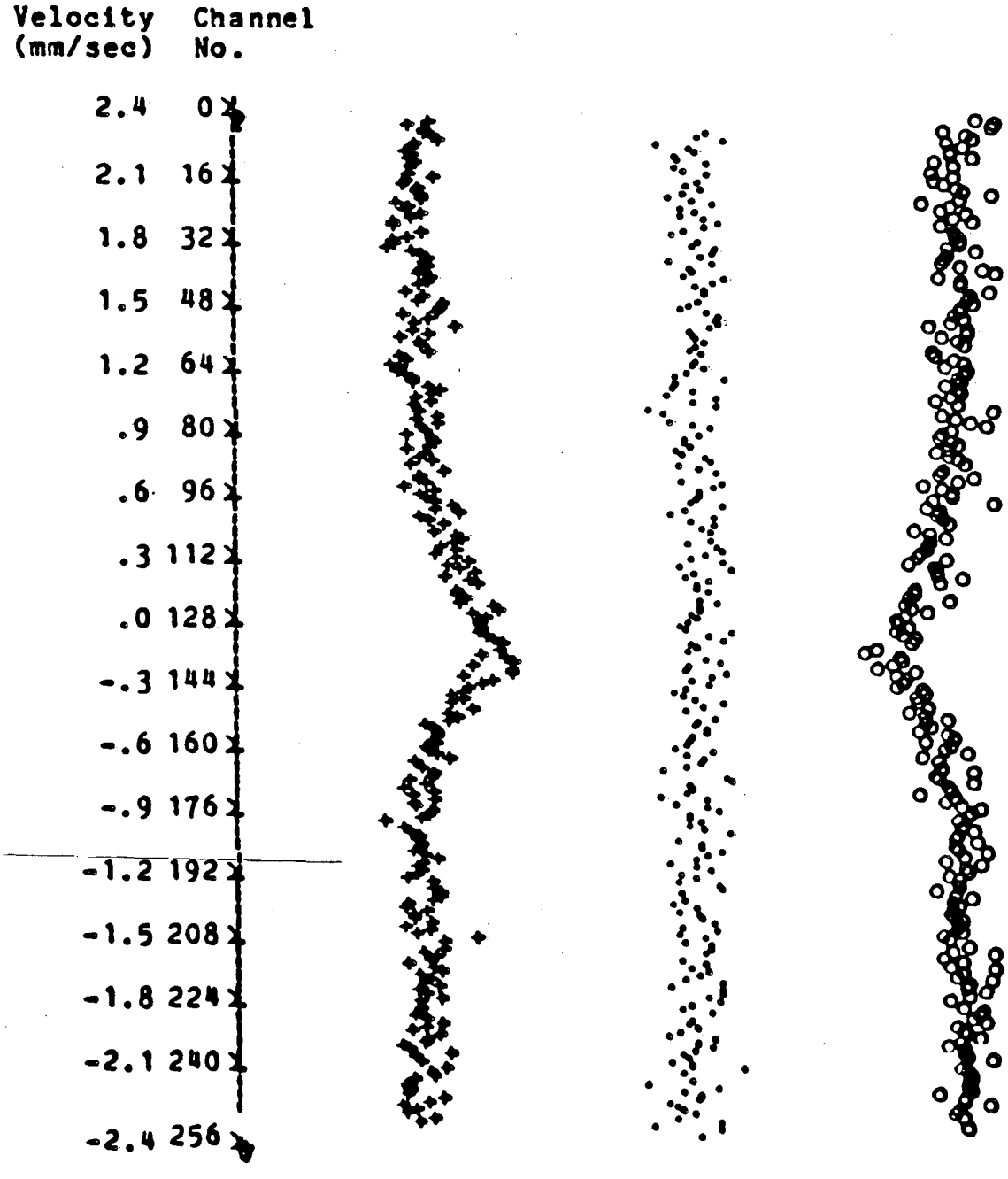

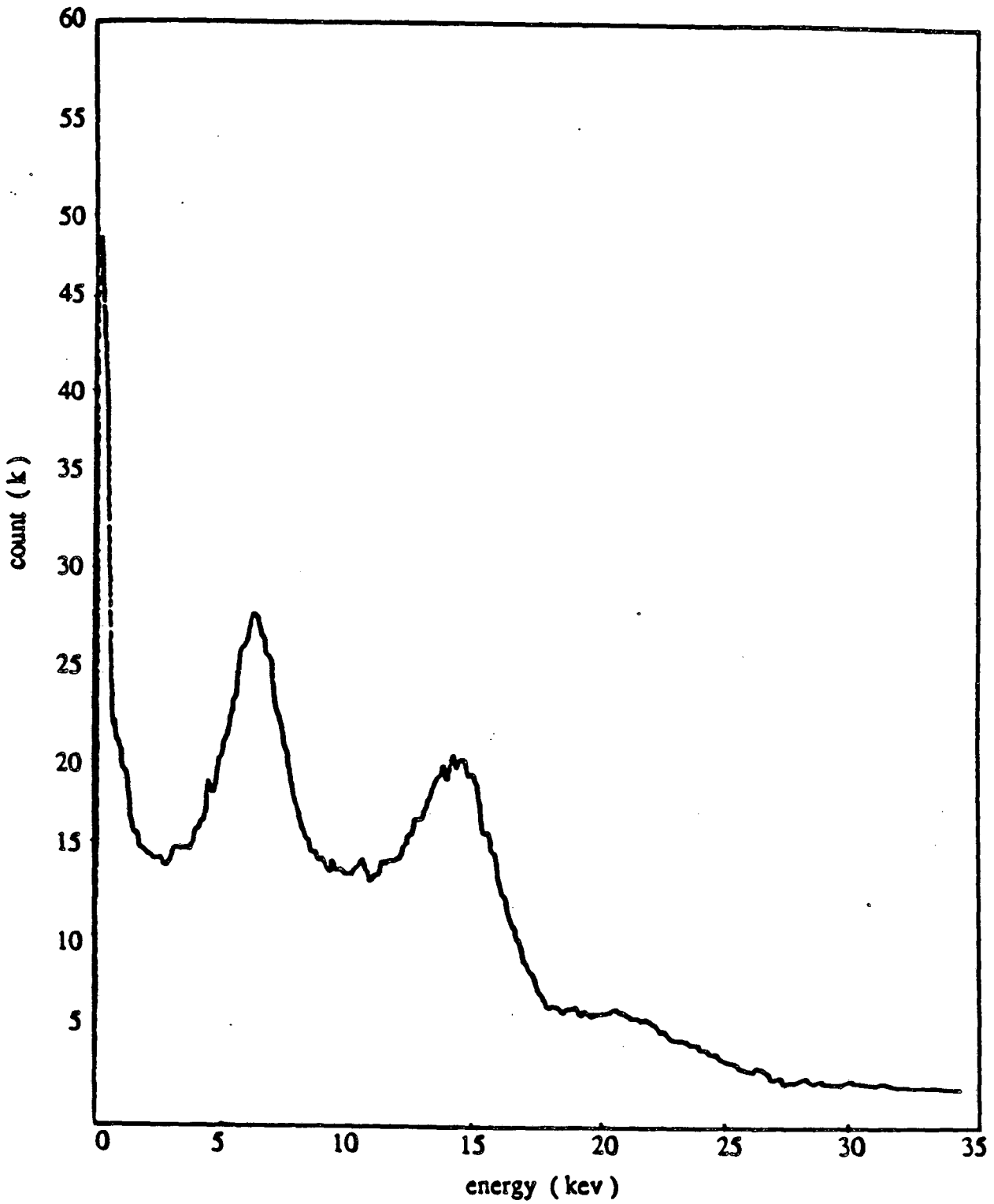

Figure 8: PHA of backscattered γ-rays by 7 mm thick Be specimen containing Fe. (Gas dector was filled with 47.5 % Ar, 47.5 % Kr, and 5 % methane, applied V = 1700 V)

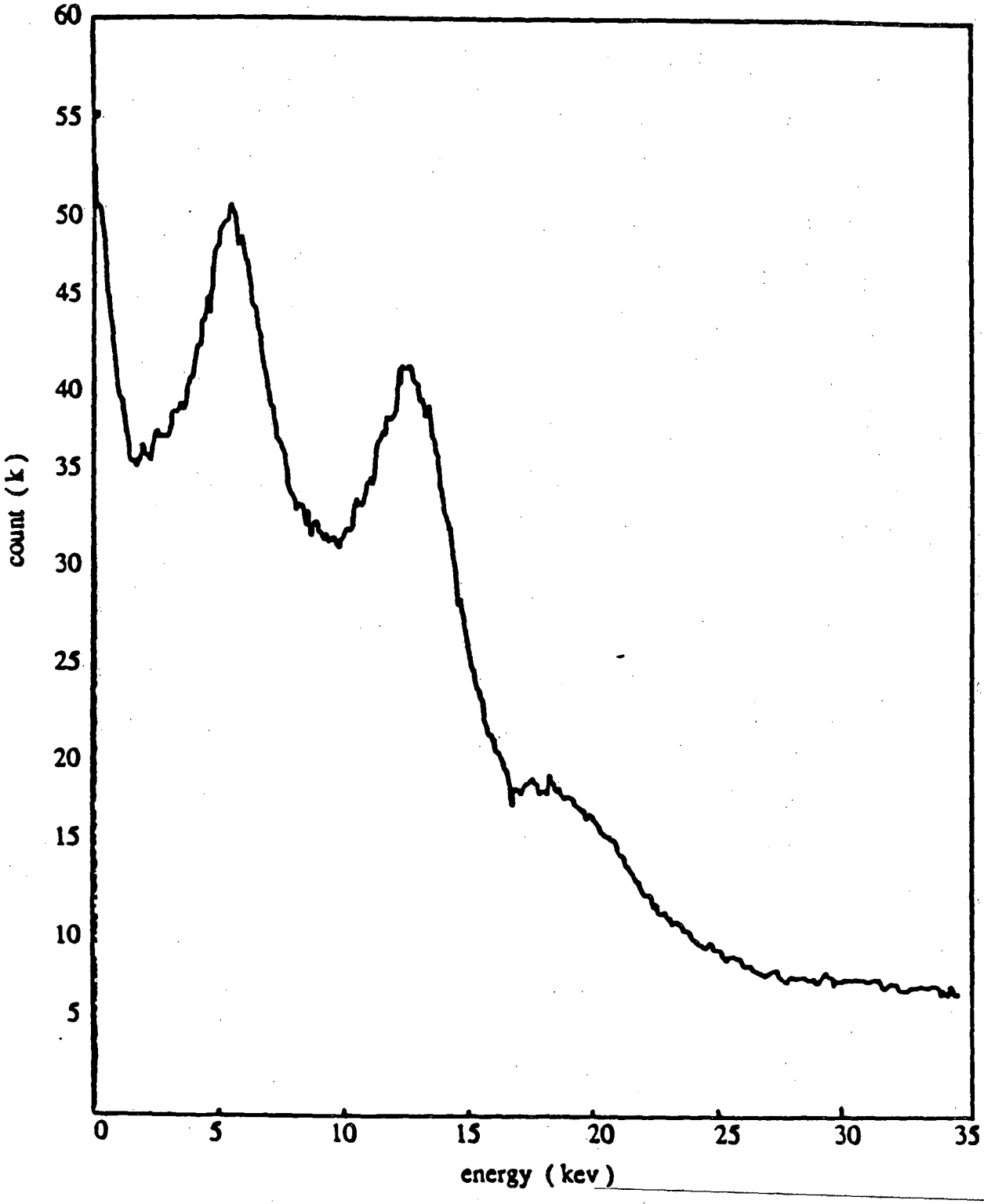

Figure 9: PHA of backscattered γ-rays by 35 mm thick Be specimen containing Fe. (Gas dector was filled with 47.5 % Ar, 47.5 % Kr, and 5 % methane, applied V = 1700 V)

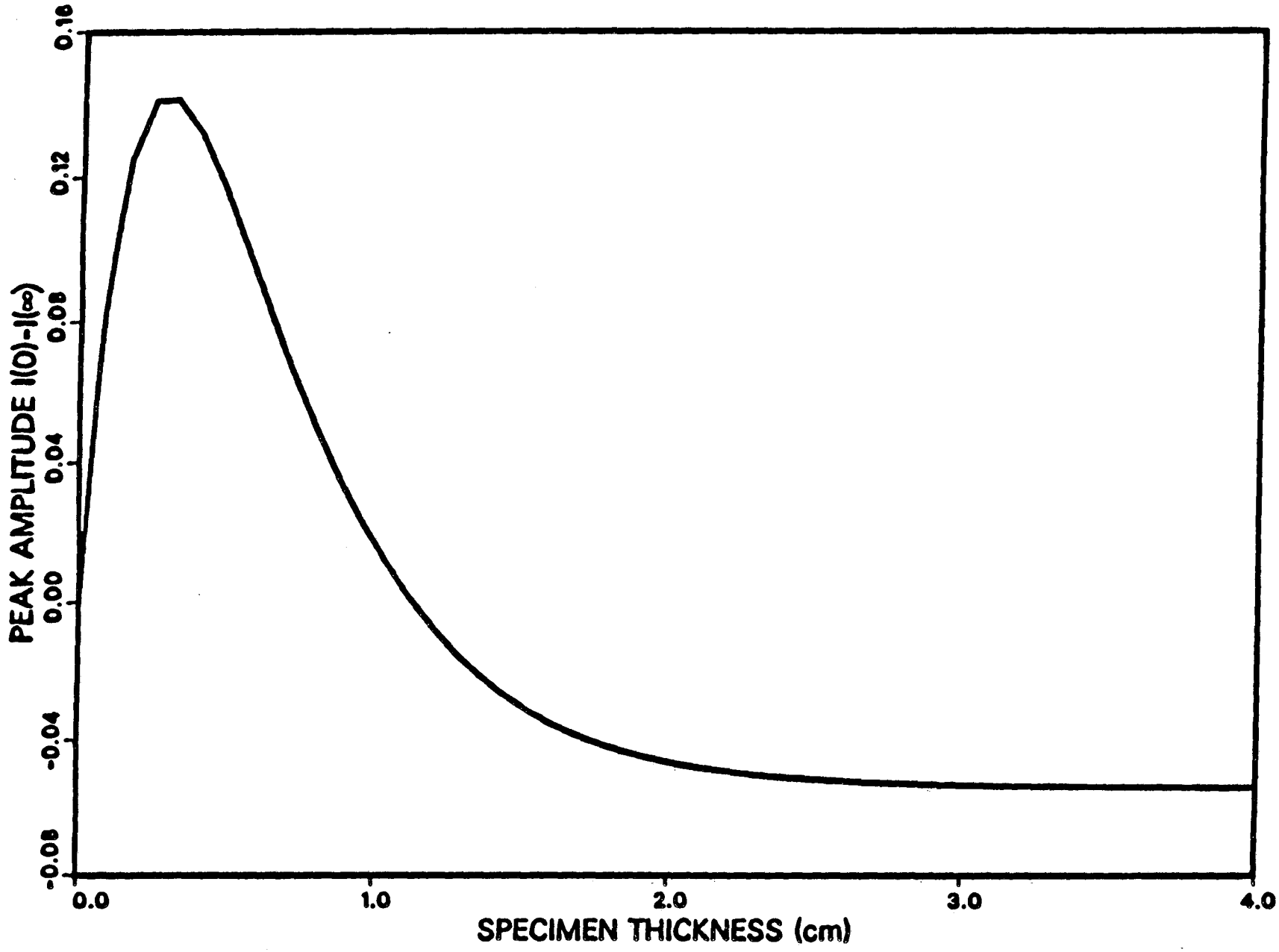

Figure 10. Numerical calculation of peak amplitude of γ-ray BMS vs scatterer thickness for Be with 0.1% (wt) natural Fe.

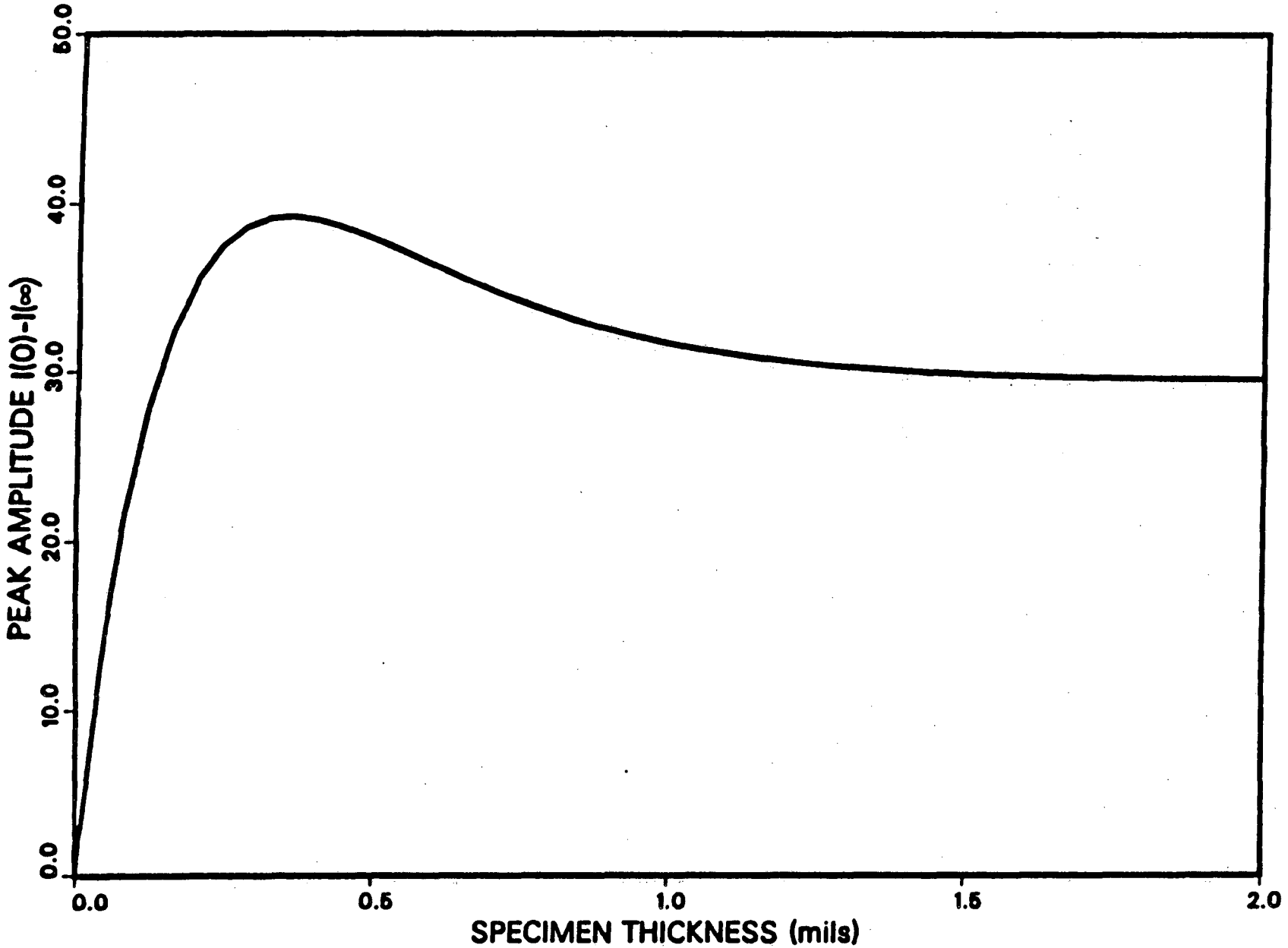

Figure 11. Numerical calculation of peak 1 amplitude of conversion X-ray BMS vs scatterer thickness of pure Fe.

TITLE FOR PLOT: BXFe009CF
BASE LINE VALUE: 133160
Y SCALE (COUNTS/IN): 8400
X SCALE (POINTS/IN): 45
MAXIMUM VELOCITY: 8.06
ZERO VELOCITY OFFSET: 0

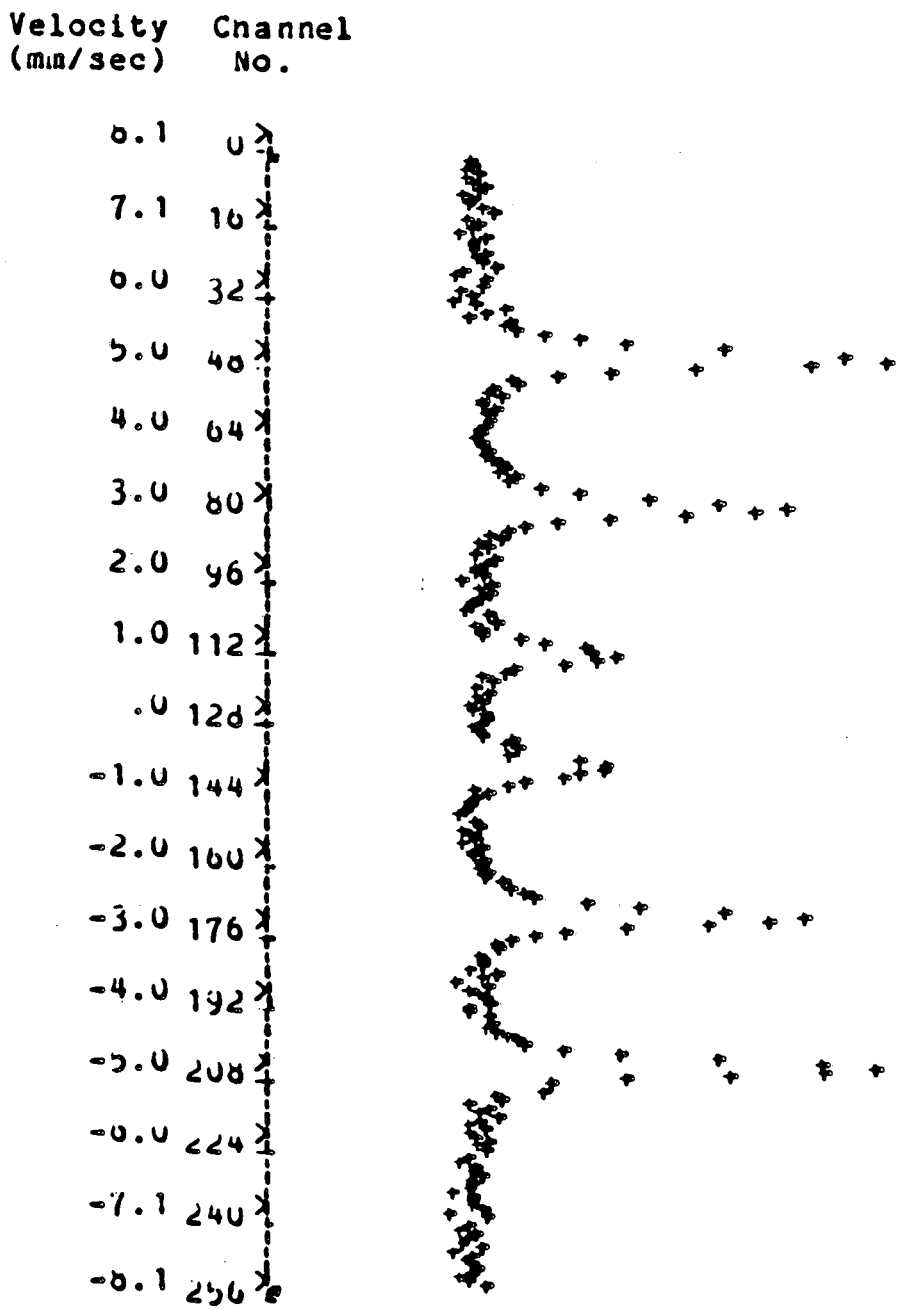

Figure 12. Conversion X-ray BMS of pure Fe with the specimen thickness of 0.1 mils.

TITLE FOR PLOT: BXFe018CF
BASE LINE VALUE: 172800
Y SCALE (COUNTS/IN): 12600
X SCALE (POINTS/IN): 45
MAXIMUM VELOCITY: 8.06
ZERO VELOCITY OFFSET: 0

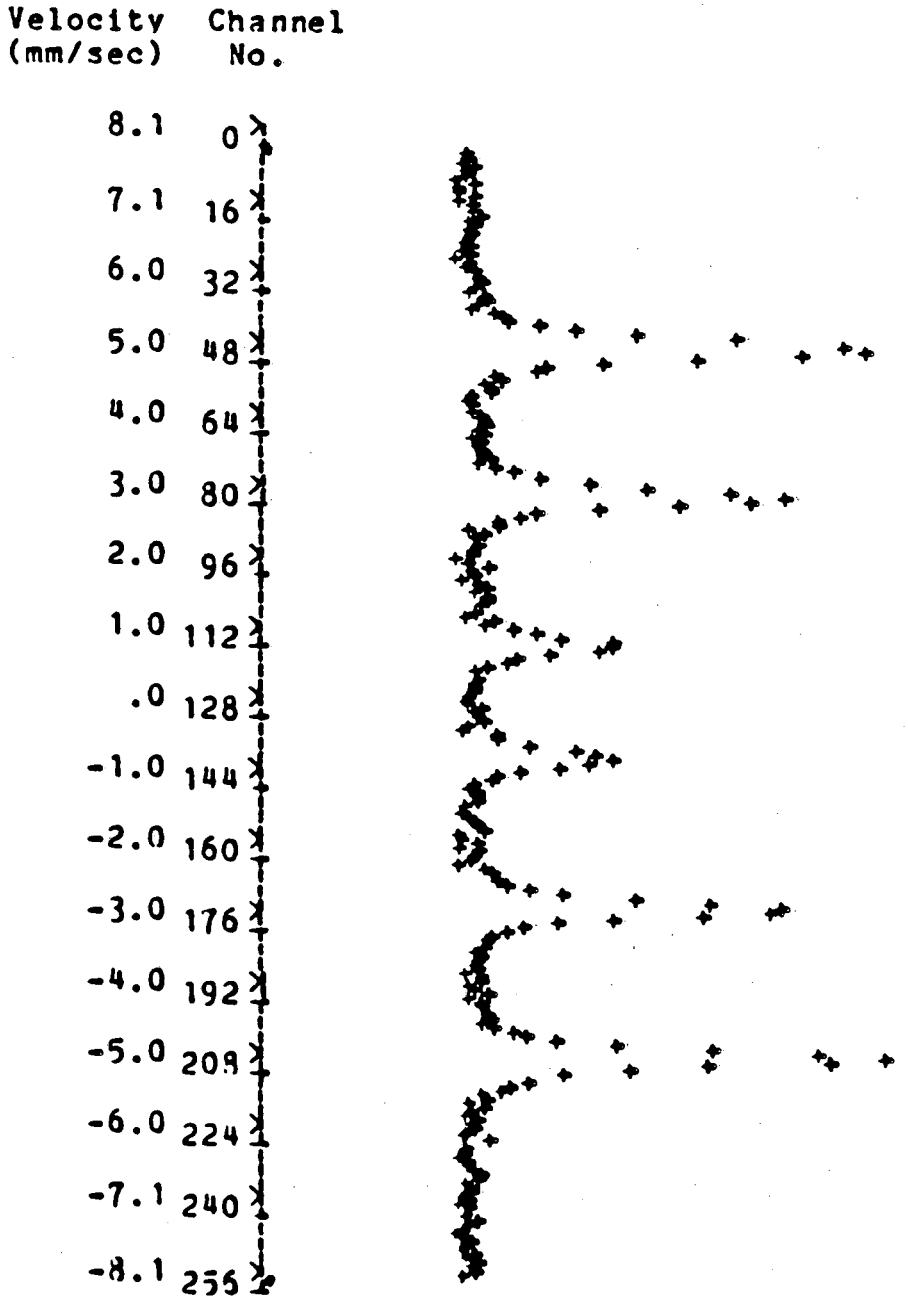

Figure 13. Conversion X-ray BMS of pure Fe with the specimen thickness of 0.2 mils.

TITLE FOR PLOT: BXFe027CF
BASE LINE VALUE: 177000
Y SCALE (COUNTS/IN): 13000
X SCALE (POINTS/IN): 45
MAXIMUM VELOCITY: 8.06
ZERO VELOCITY OFFSET: 0

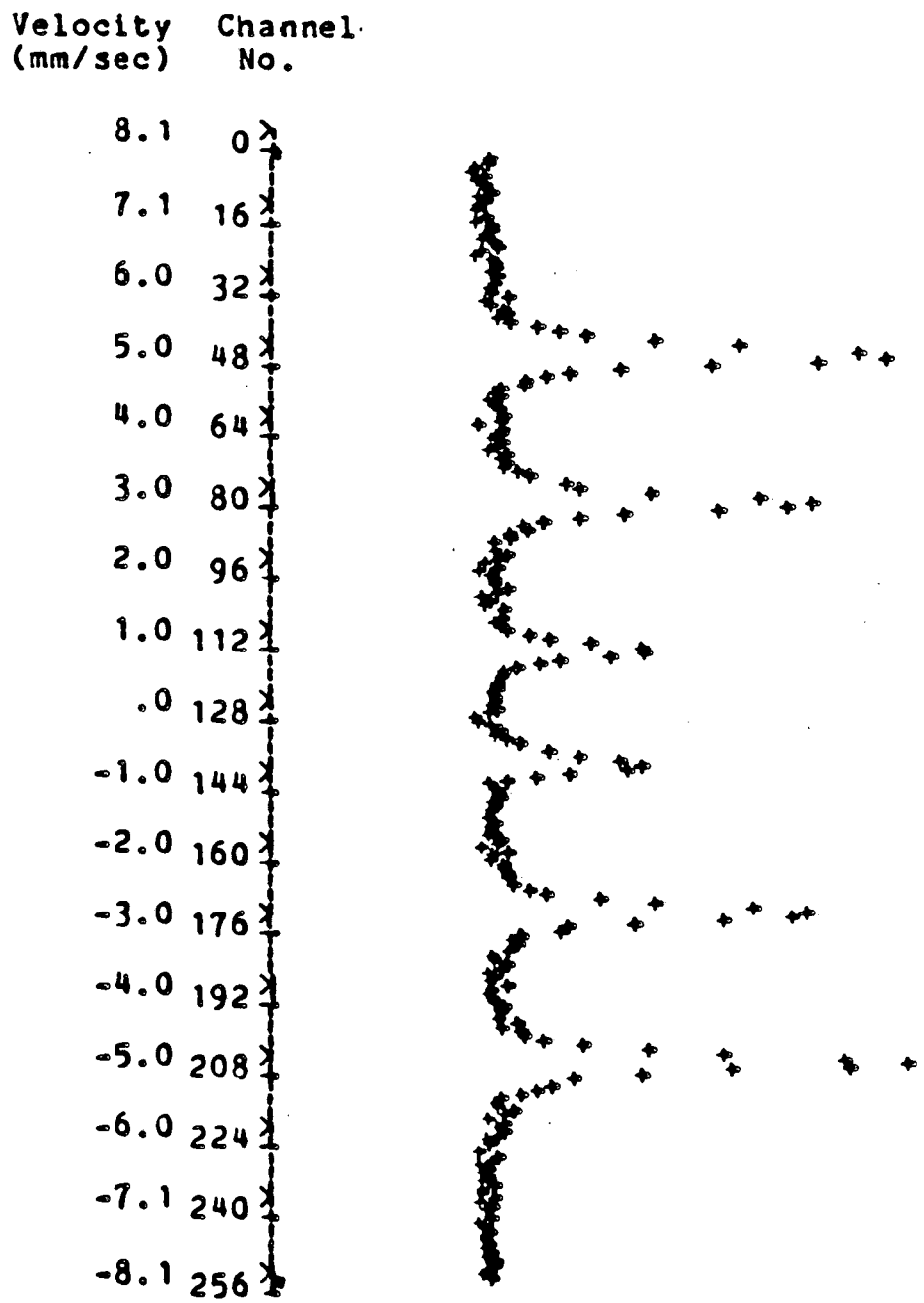

Figure 14. Conversion X-ray BMS of pure Fe with the specimen thickness of 0.3 mils.

TITLE FOR PLOT: BXFe047CF
BASE LINE VALUE: 194000
Y SCALE (COUNTS/IN): 14000
X SCALE (POINTS/IN): 45
MAXIMUM VELOCITY: 8.06
ZERO VELOCITY OFFSET: 0

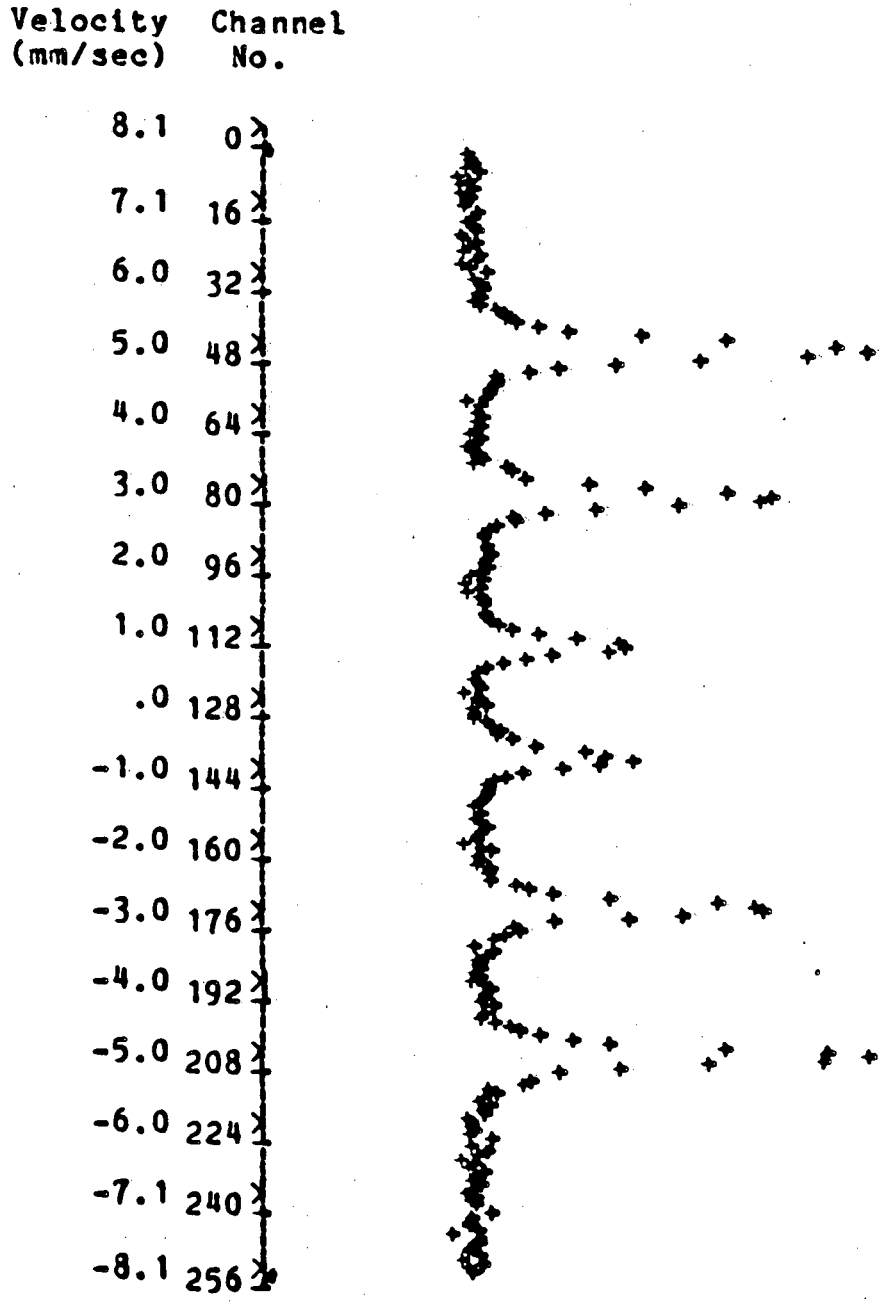

Figure 15. Conversion X-ray BMS of pure Fe with the specimen thickness of 0.47 mils.

TITLE FOR PLOT: BXFe080CF
BASE LINE VALUE: 210400
Y SCALE (COUNTS/IN): 16000
X SCALE (POINTS/IN): 45
MAXIMUM VELOCITY: 8.06
ZERO VELOCITY OFFSET: 0

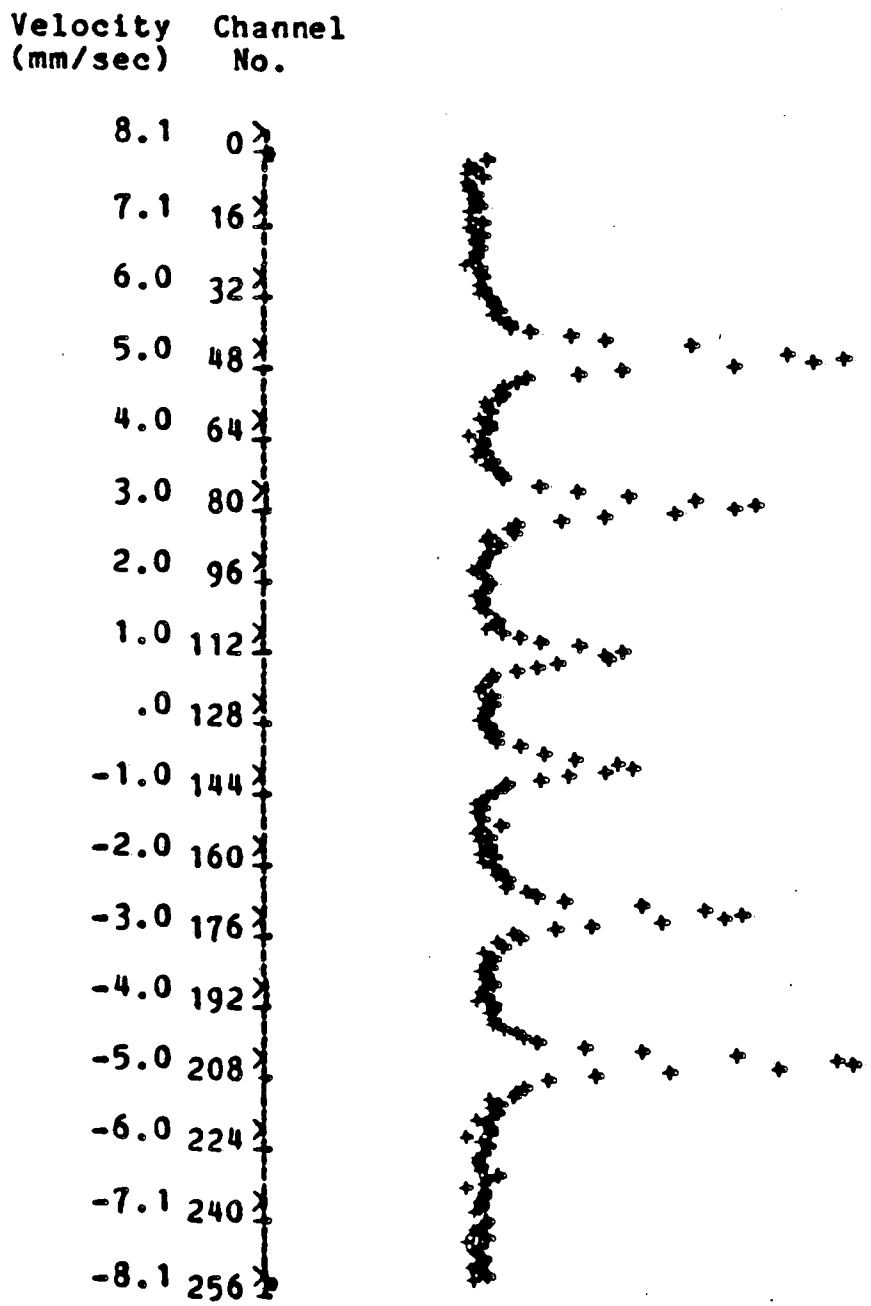

Figure 16. Conversion X-ray BMS of pure Fe with the specimen thickness of 0.82 mils.

TITLE FOR PLOT: BXFe113CF
BASE LINE VALUE: 304454
Y SCALE (COUNTS/IN): 19900
X SCALE (POINTS/IN): 45
MAXIMUM VELOCITY: 8.06
ZERO VELOCITY OFFSET: 0

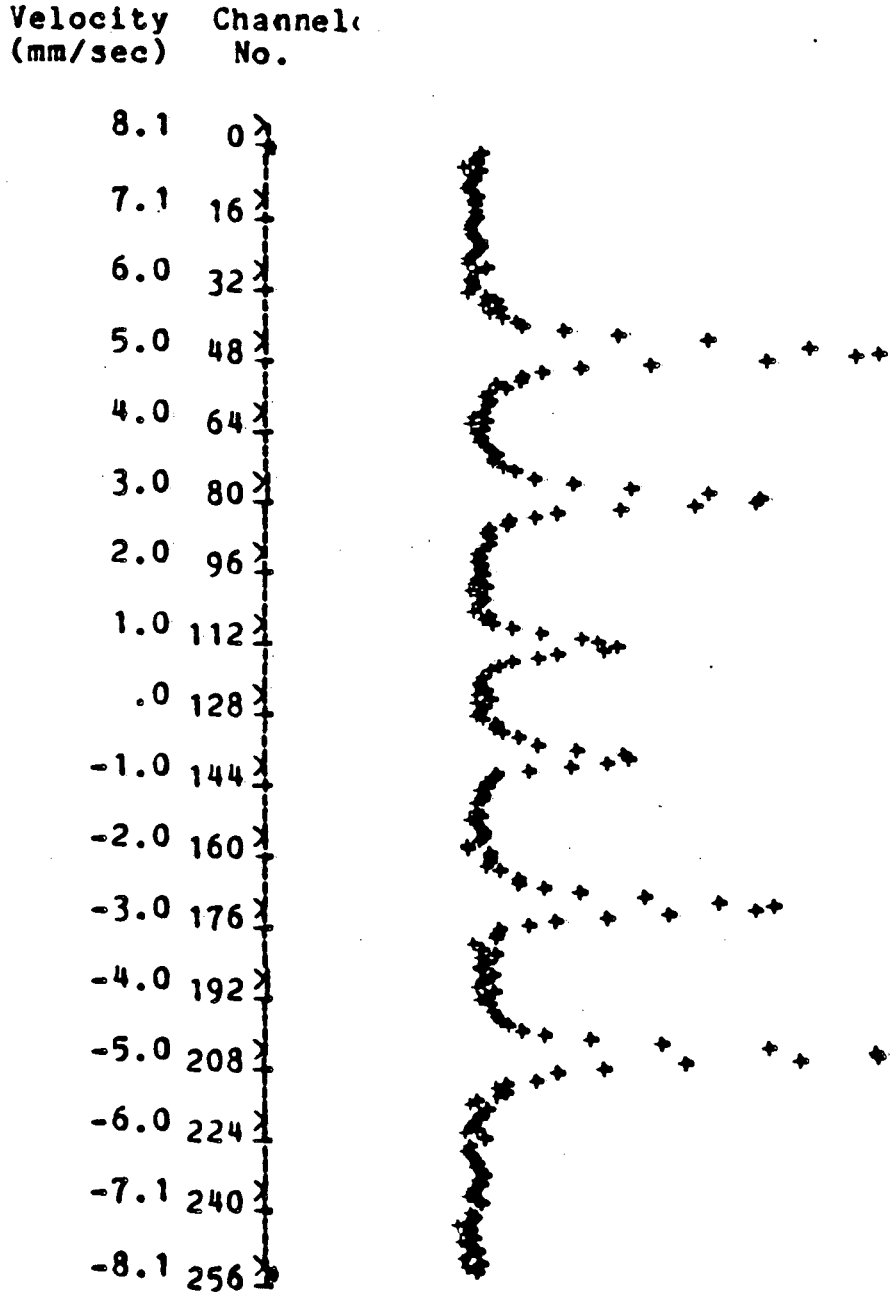

Figure 17. Conversion X-ray BMS of pure Fe with the specimen thickness of 1.13 mils.

TITLE FOR PLOT: BXFe213Cr
BASE LINE VALUE: 222764
Y SCALE (COUNTS/IN): 13746
X SCALE (POINTS/IN): 45
MAXIMUM VELOCITY: 8.06
ZERO VELOCITY OFFSET: 0

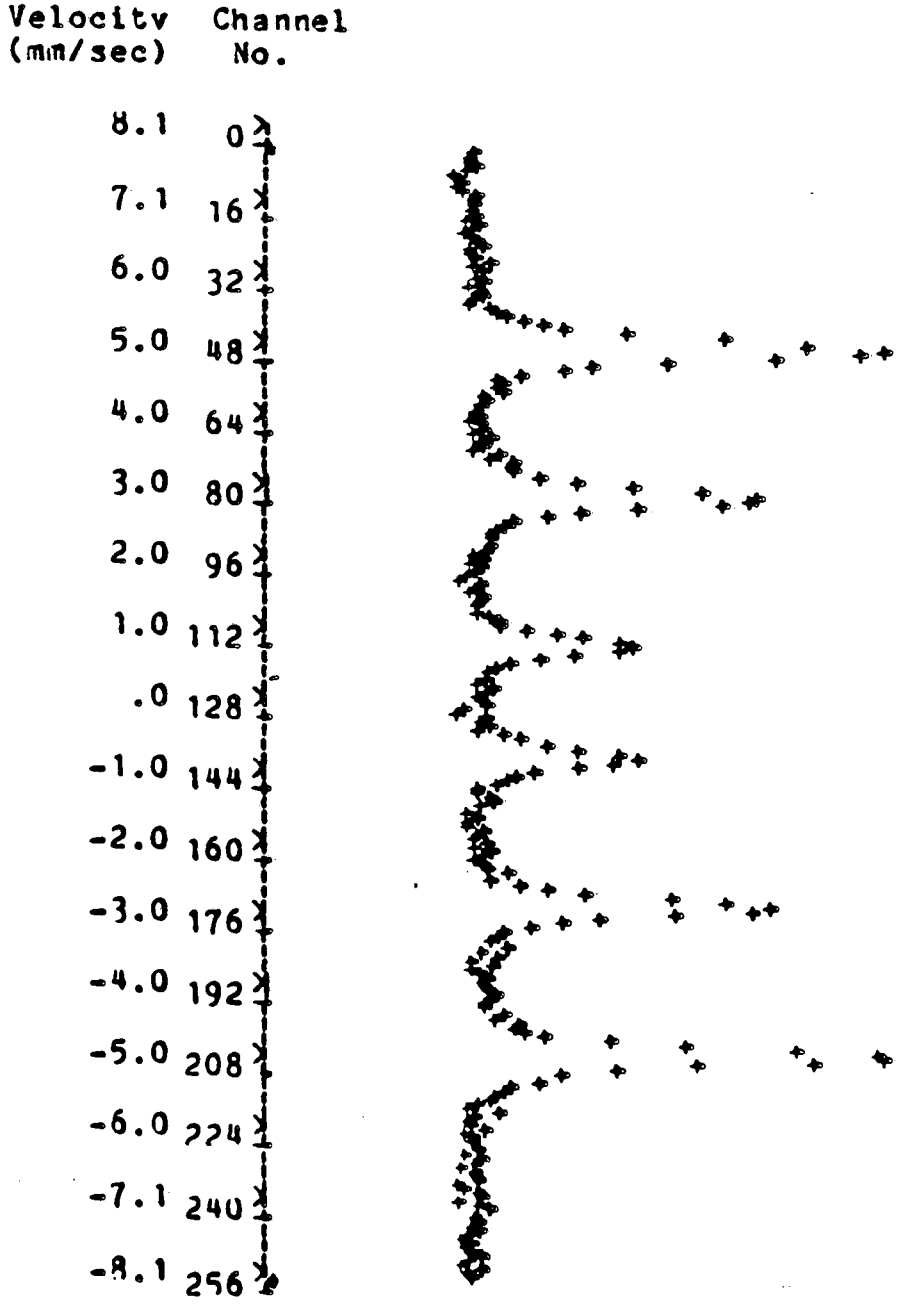

Figure 18. Conversion X-ray BMS of pure Fe with the specimen thickness of 2.23 mils.

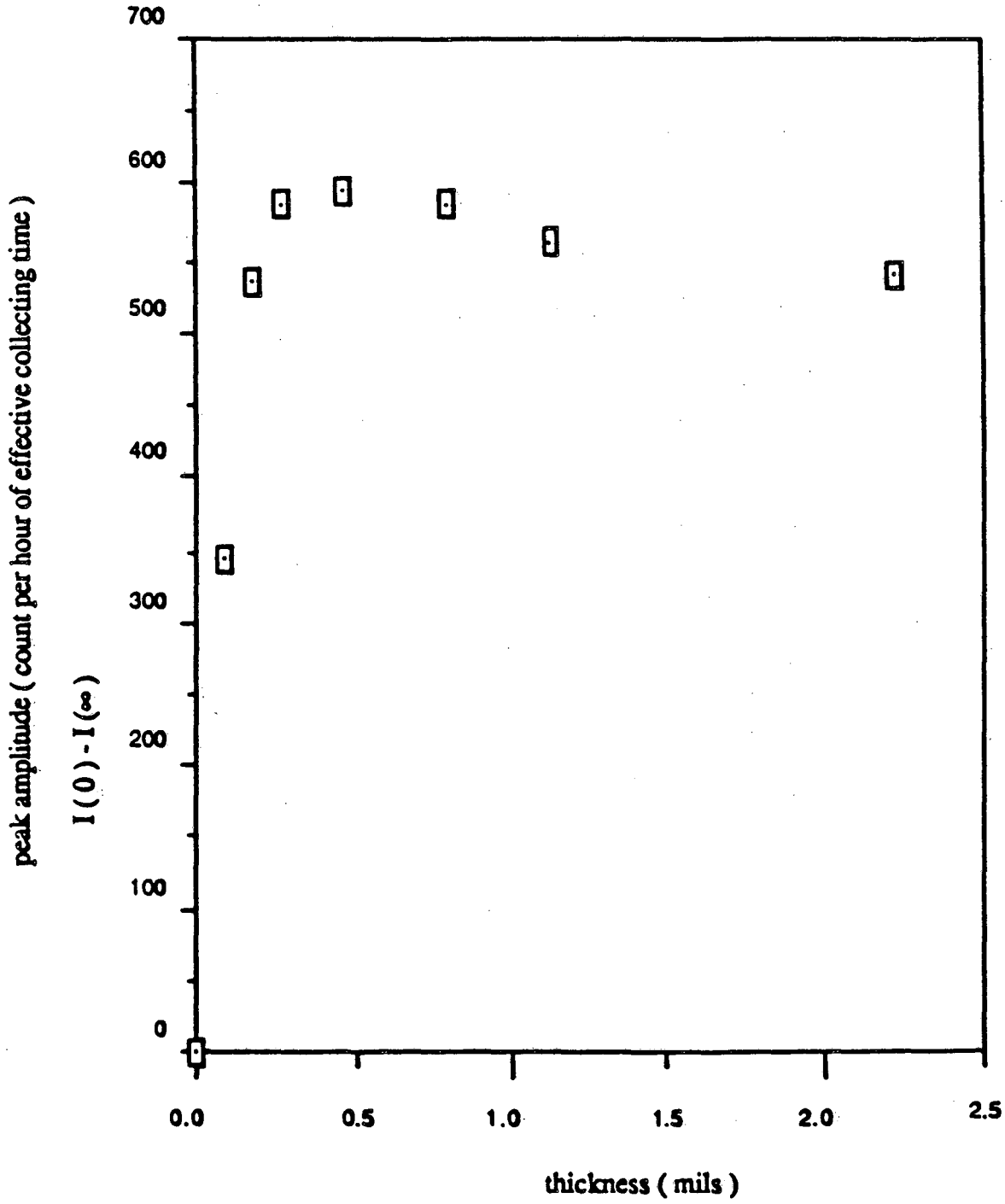

Figure 19. Experimental data of peak amplitude vs. scatterer thickness. (Peak amplitude plotted were calculated by averaging the amplitudes of peak 1 and peak 6 in the Fe sextet spectrum.)

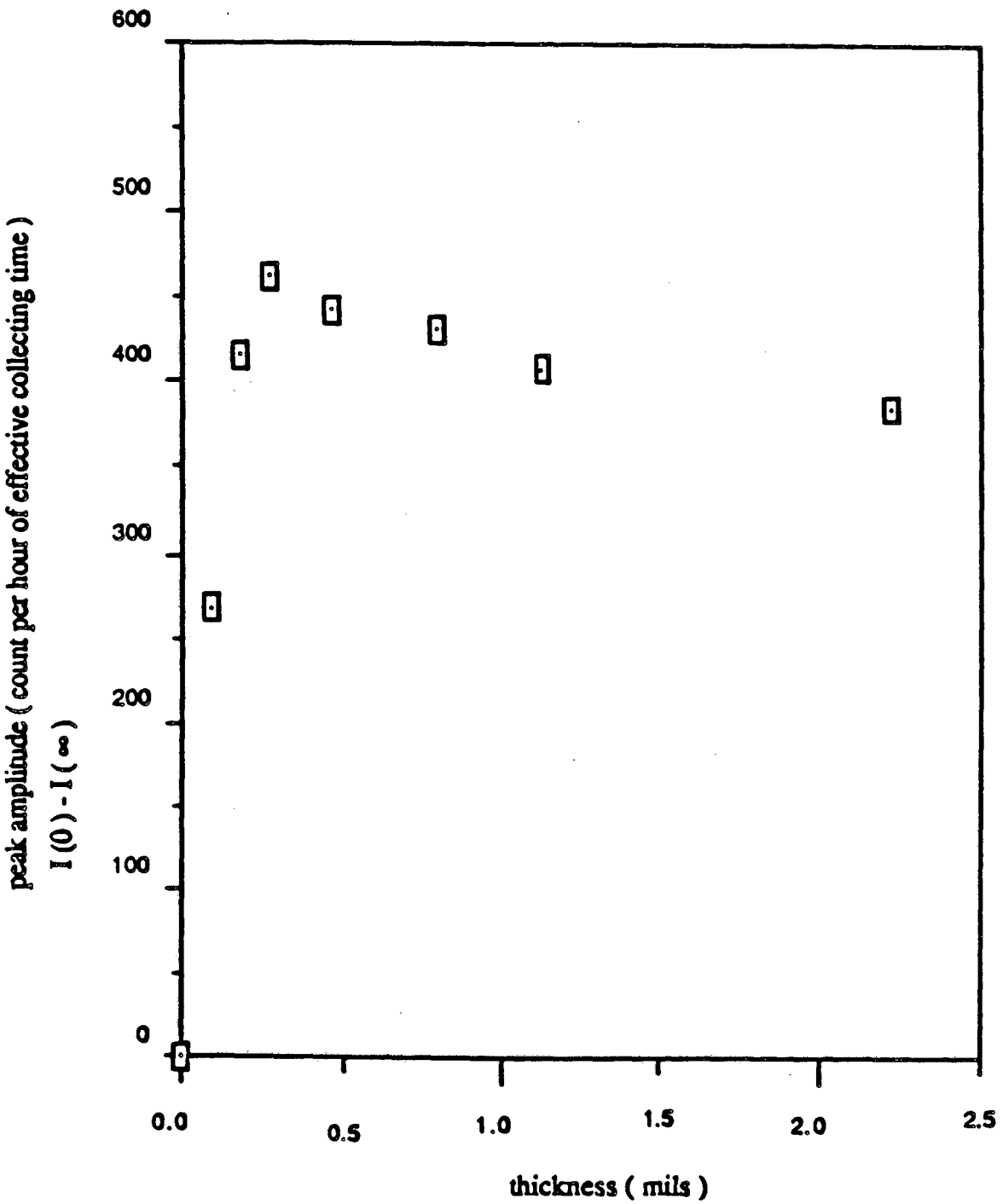

Figure 20. Experimental data of peak amplitude vs. scatterer thickness. (Peak amplitude plotted were calculated by averaging the amplitudes of peak 2 and peak 5 in the Fe sextet spectrum.)

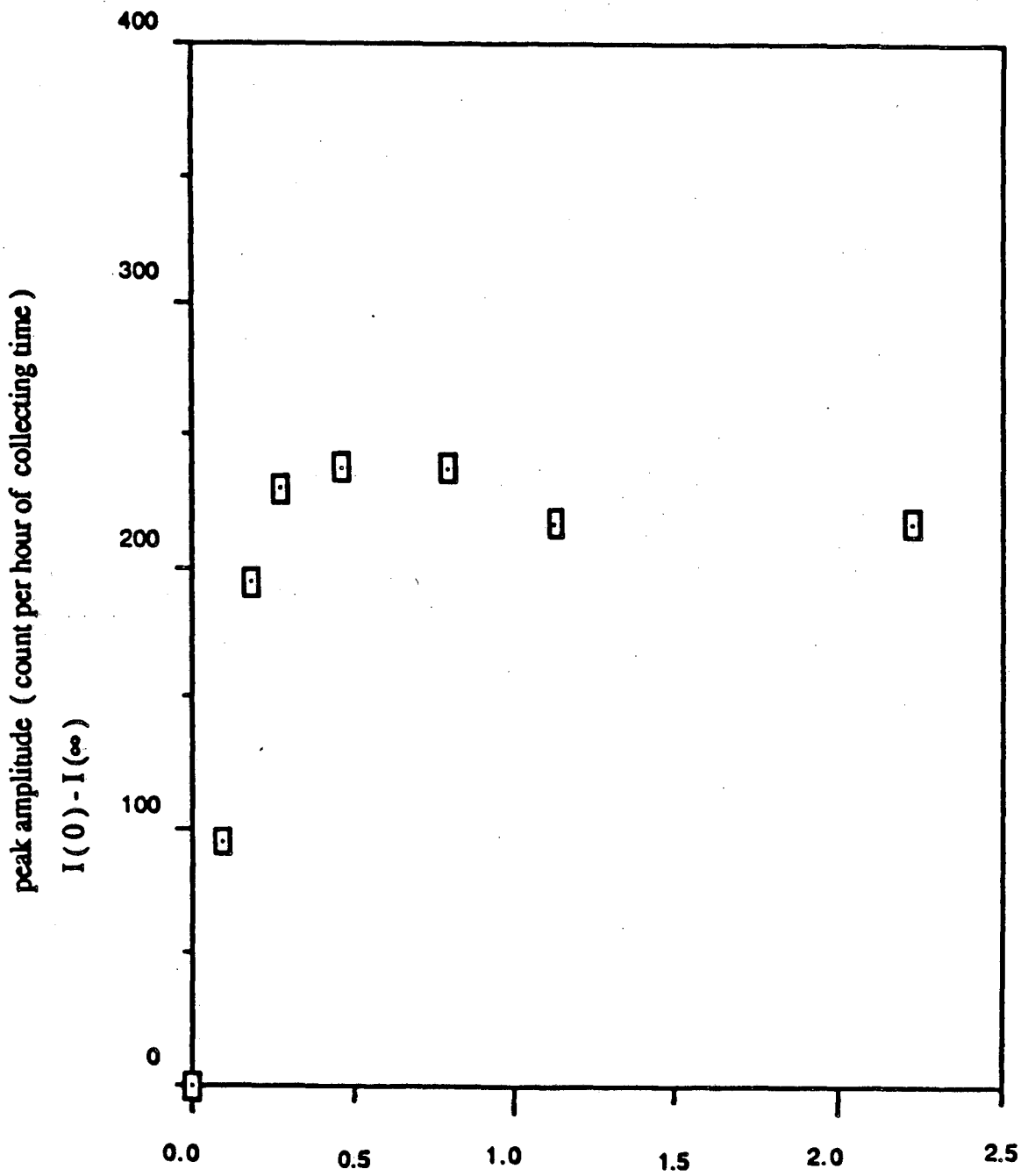

Figure 21 Experimental data of peak amplitude vs. scatterer thickness. (Peak amplitude plotted were calculated by averaging the amplitudes of peak 3and peak 4 in the Fe sextet spectrum.)

LAWRENCE BERKELEY LABORATORY
TECHNICAL INFORMATION DEPARTMENT
UNIVERSITY OF CALIFORNIA
BERKELEY, CALIFORNIA 94720